# TIP EFFECTS ON FLUCTUATING LIFT AND DRAG FORCES ACTING ON A CIRCULAR CYLINDER PERPENDICULAR TO AN AIR FLOW

Thesis by

Harry Spencer Blackiston, Jr.

In Partial Fulfillment of the Requirements

For the Degree of

Aeronautical Engineer

California Institute of Technology

Pasadena, California

1963

## ACKNOWLEDGMENT

The author would like to express his appreciation to Dr. Y. C. Fung for the guidance and motivation given while this work was performed, to the National Science Foundation for support via a research grant, and to the Lockheed Aircraft Corporation for a fellowship. L. V. Schmidt, M. E. Jessey, and R. D. Luntz, through their advice and assistance, enhanced the acquisition of test data and its subsequent analog reduction. W. H. Bettes, Jr., W. L. McNay, E. S. Lapworth, and R. Gauthier facilitated the setting up of test conditions. Misses Helen Burrus and Jeanette Siefke aided ably in the manuscript preparation. My wife, Rosa Lee, provided steady encouragement and unfailing moral support.

## ABSTRACT

Tests were conducted to evaluate the tip effects on the local air loads that act on a circular cylinder normal to a flow at Reynolds numbers, based on cylinder diameter, of $0.38 \times 10^6$, $0.53 \times 10^6$, $0.65 \times 10^6$ and $0.75 \times 10^6$ (corresponding to wind tunnel dynamic pressures of 10, 20, 30, and 40 psf, respectively). Tip configurations consisted of a blunt-end (or smokestack), a hemisphere, a 15 degree half-angle cone, and an ellipsoid with semi-major axis of 1.5 cylinder diameters. Localized boundary layer tripping facilitated controlled disturbances near the tip.

Unsteady lift and drag were significantly altered by the hemispherical and ellipsoidal ends as compared with the blunt-end. In contrast, the conical tip showed much smaller changes. Local lift and drag coefficients, as well as cross-correlation coefficients, vary rapidly along the cylinder axis near the tip.

The importance of boundary layer characteristics on the fluctuating forces was demonstrated by boundary layer tripping with air blowing out through suitably located orifices in the cylinder.

TABLE OF CONTENTS

LIST OF FIGURES

LIST OF FIGURES (cont'd.)

# NOTATION

## A. List of Symbols

| | |
|---|---|
| $D$ | Diameter of cylinder |
| $f$ | Frequency, cycles per second |
| $q$ | Dynamic pressure, $= 1/2\ \rho V^2$ |
| $t$ | Time |
| $V$ | Velocity of undisturbed flow |
| $X$ | Axial coordinate along cylinder axis, $X = 0$ at blunt-end, the origin being fixed in space regardless of the addition of nose shapes or shaker |
| $\theta$ | Angular coordinate for cylinder surface, referenced at forward stagnation point |
| $\nu$ | Kinematic viscosity of fluid |
| $\rho$ | Mass density of fluid |
| $\chi$ | Correlation length, dimensionless |

All other symbols are defined in the text as they arise.

## B. Superscripts

$$\text{Mean average, } = \lim_{T \to \infty} \frac{1}{2T} \int_{-T}^{+T} (\ )\, dt$$

C. Subscripts

$( )_{\ell^2}$ Refers to lift at station $X_1$ and to lift at station $X_2$

$( )_{d^2}$ Refers to drag at station $X_1$ and to drag at station $X_2$

$( )_{\ell_j}$ Refers to lift at station $X_j$

$( )_{d_j}$ Refers to drag at station $X_j$

D. Coefficients

$C_\ell$ Local lift force coefficient, $= \frac{\text{Lift force/unit span}}{qD}$

$C_d$ Local drag force coefficient, $= \frac{\text{Drag force/unit span}}{qD}$

Re Reynolds number of cylinder, $= \frac{VD}{\nu}$

S Strouhal number (non-dimensional frequency), $= \frac{fD}{V}$

# I. INTRODUCTION

Much work has been done in past years on the lift and drag stemming from the flow past a circular cylindrical structure whose longitudinal axis is normal to the flow. Goldstein's book (1) contains a review of the theoretical and experimental results up to about 1937. Humphrey's thesis (2) presents a review of later works up to about 1959. Further references to the fluctuating loads acting on large cylindrical structures such as smokestacks and missiles are given by Fung (3, 5). In earlier investigations summarized in the literature referred to above, only passing attention was given to the three-dimensional aspects of the fluctuating air loads. This particular feature of the unsteady lift on a two-dimensional cylinder model was reported by Fung (3) and Macovsky (6) in 1958, and emphasized by Humphreys (2) in 1959. The effects on unsteady loads of the axial location of chordwise fences on a circular cylinder were discussed by Keefe (7) in 1961. Investigators have noted interference effects in the region where a cylinder passes through a wind tunnel wall or floor, e.g., Humphreys (2) and Gerrard (8, 9). Delaney and Sorensen (10) mention qualitatively the results of tests on cylinders where the models passed through unsealed openings in the tunnel walls. Ezra and Birnbaum (12) indicated the strong influence of nose shape on the root bending moment of large missiles acted upon by unsteady loads.

There was specific need for careful and detailed investigation of end effects and axial correlations of fluctuating forces. The present

work is part of a continuing effort at the GALCIT* in determining the fluctuating lift and drag forces acting on cylinders for the purpose of describing the structural response of cylindrical structures. The basic stochastic features, and the form of statistical averages required for response analyses were examined by Fung (See Refs. 3, 4, and 5). The improved measurements, using pressure cells instead of force transducers were made by Schmidt (11). The intent of the present study is to extend the work reported in reference 11 concerning the axial correlation of the unsteady air loads for a blunt-end cylinder and to outline the effects of selected tip shapes on local air loadings near the model tip.

---

* Graduate Aeronautical Laboratories, California Institute of Technology.

## II. OUTLINE OF EXPERIMENTS AND DESCRIPTION OF APPARATUS

The object of the experimental portion of this study was the measurement of local aerodynamic forces on a cantilevered circular cylinder normal to a flow at Reynolds numbers, based on cylinder diameter, of $0.38 \times 10^6$, $0.53 \times 10^6$, $0.65 \times 10^6$ and $0.75 \times 10^6$ (corresponding to wind tunnel dynamic pressures of 10, 20, 30, and 40 psf, respectively). Configurations included the basic blunt-end (or smokestack), and departures therefrom, described as follows (Figures 1 to 5):

1. Cylinder model with hemispherical tip, nominal 15 degree half-angle cone 2.0 cylinder diameters long, and ellipsoidal tip of semi-major axis of 1.5 cylinder diameters,

2. Smokestack configuration with localized boundary layer tripping near the tip,

3. Smokestack configuration with shaker mounted internal to the cylinder at the tip.

A schematic of the basic installation and a graph of the tunnel operating range are shown in Figures 6 and 7.

The blunt-end cylinder model (8.54 inch diameter) protruded vertically 8.07 diameters from the floor of the GALCIT Ten-Foot Wind Tunnel test section. Loads were measured simultaneously at two stations via instrumented cylinder sections, hereafter called Channels 1 and 2. Channel 1 was always between Channel 2 and the free end of the cylinder (See Figure 9). The sections could be rotated such that both sensed drag forces or both sensed lift forces. The dynamic

response traits of the instrumented sections were such that measurements below 200 cps did not require a response correction. The range of interest of observed frequencies is less than this number. Figure 8 shows a schematic of an instrumented section.

A detailed description of the model, air blowing apparatus, instrumentation, and logic involved in the choice of instrumentation is given in reference 11.

The shaker consisted of a flywheel, belt-driven by a 1/10 Hp blower motor (See Figure 5 for details). An 18 gram weight was attached to the flywheel 1.75 inches from the axis of rotation. The shaker and its cover added 1.4 cylinder diameters to the length of the basic smokestack.

The model tips were turned from hardwood blocks (laminations of one inch thickness) and each was fixed to an aluminum mounting plate.

# III. DATA HANDLING

## 3.1 Data Recording

The data recorded were the output of the two carrier amplifier channels, which were electrical analogs of the localized air loads, and the output of two strain gage type accelerometers. One accelerometer was firmly attached to each of the instrumented cylinder sections, Channels 1 and 2. When these sections both sensed local lift forces, the accelerometers both sensed local motion of the cylinder model in the lift direction. Similarly, when the sections both sensed local drag forces, the accelerometers sensed local motion of the cylinder model in the drag direction.

The data recording system is shown schematically in Figure 9. An Ampex FR-100 frequency modulated (FM) tape recorder registered the data, cited in the preceding paragraph, on one inch wide magnetic tape. Known voltages in the range $\pm$ 1.4 volts DC., and zeroes were recorded before and after runs of data-taking to enable proper referencing upon subsequent playback of taped data. Data were monitored after passage through amplifiers, at the input point into the recorder, and after playback from the tape. This prevented introduction of random peaks and shifts in DC. levels in the tape recorder input signals which might exceed the linear range of the recorder channels.

With average tape recorder performance in a linear manner, proper data monitoring, and careful calibration of equipment, taped data will facilitate accuracy of signal voltages to about 1 per cent of full range or $\pm$ 0.015 volts.

Added details of the data recording procedure are described in reference 11.

Typical time traces of the lift forces acting on the smokestack and hemispherical tip are shown in Figures 10 and 11. The data were played back from magnetic tape wherein the tape recorder output was run through an Offner Type P two channel recording oscillograph. Traces for drag are similar but with, in general, a greater rate of fluctuation of the signals.

## 3.2 Data Reduction by Analog Methods

Correlation coefficients, as defined in Section 4.1, were obtained from analysis of taped data by analog techniques. A schematic of the process and related equipment is shown in Figure 12. The taped signals from Channels 1 and 2, when played back, are in the form of two voltages, $e_1(t)$ and $e_2(t)$, respectively. Thus, if the instrumented sections had sensed lift, then $e_1(t)$ is analogous to the local lift, $\mathscr{l}(X_1, t)$, and $e_2(t)$ is analogous to the local lift, $\mathscr{l}(X_2, t)$. The Philbrick K5M multiplier was used to obtain cross products and squares of the voltages, $e_1(t)$ and $e_2(t)$. The Philbrick UPA-2 operational amplifier was part of an averaging circuit (See Figure 12c) used to obtain, with respect to time, the means of $e_1(t)$ and $e_2(t)$ as well as their mean squares and mean cross products. Constants in the averaging circuit were chosen to yield a static voltage gain of about -7.5 and a time constant of 9 seconds. This time constant smoothed the data to a certain extent and corresponded to the time period used to get the averages of $e_1(t)$ and $e_2(t)$.

Initial plots consisted of $\overline{e_1(t)}$ and $\overline{e_2(t)}$, the time averages of the voltages, $e_1(t)$ and $e_2(t)$, respectively. These averages were approximately set to zero over a common period of at least 10 seconds. This was done by shifting the DC. levels of the signals through use of the "bucking" voltage applied to one of the two input grids of the Epsco differential amplifier (See Figure 12). Graphs were then made of $\overline{e_1^2(t)} + \left[\overline{e_1(t)}\right]^2$, $\overline{e_2^2(t)} + \left[\overline{e_2(t)}\right]^2$ and $\overline{e_1(t)e_2(t)} + \left[\overline{e_1(t)}\right]\left[\overline{e_2(t)}\right]$. To assure reliable results from the analog data reduction system, frequent checks were made of the calibrations of the Philbrick K5M multiplier and UPA-2 operational amplifier.

# IV. RESULTS AND DISCUSSION

## 4.1 Axial Correlation

A distinctive element in the description of a random process is the cross-correlation coefficient. The nature of the measurements described herein lends itself to this concept since loads were sensed locally and can be thought to act at a point along the cylinder axial coordinate.

In general, the lift as a function of time at a station $X_j$ is designated as $\ell(X_j, t)$, $j = 1, 2$. Using the notation of Fung (5), defining the mean value, $\overline{\ell(X_j, t)}$, $= 0$, the cross-correlation coefficient for the lift is given by

$$R_{\ell 2} = \frac{\overline{\ell(X_1, t)\, \ell(X_2, t)}}{\left[\overline{\ell^2(X_1, t)}\right]^{1/2} \left[\overline{\ell^2(X_2, t)}\right]^{1/2}}$$

where

$\overline{\ell(X_1, t)\, \ell(X_2, t)}$ = mean, with respect to time, of the product of the stochastic processes, $\ell(X_1, t)$, $\ell(X_2, t)$,

$\overline{\ell^2(X_1, t)}$, $\overline{\ell^2(X_2, t)}$ = mean square values of $\ell(X_1, t)$ and $\ell(X_2, t)$.

Following Fung (5), the drag at station $X_j$ is defined as

$$d(X_j, t) = d_0(X_j) + d_1(X_j, t)$$

where

$d_o(X_j)$ = steady component of drag at $X_j$

$d_1(X_j, t)$ = fluctuating component of drag at $X_j$

By definition $\overline{d_1(X_j, t)} = 0$. The cross-correlation coefficient for drag is given by

$$R_{d^2} = \frac{\overline{d(X_1, t)\, d(X_2, t)}}{\left[\overline{d^2(X_1, t)}\right]^{1/2} \left[\overline{d^2(X_2, t)}\right]^{1/2}}$$

$$= \frac{d_o(X_1)\, d_o(X_2) + \overline{d_1(X_1, t)\, d_1(X_2, t)}}{\left[d_o^2(X_1) + \overline{d_1^2(X_1, t)}\right]^{1/2} \left[d_o^2(X_2) + \overline{d_1^2(X_2, t)}\right]^{1/2}}$$

where

$\overline{d(X_1, t)\, d(X_2, t)}$, $\overline{d_1(X_1, t)\, d_1(X_2, t)}$ = mean, with respect to time, of the products, $d(X_1, t)\, d(X_2, t)$ and $d_1(X_1, t)\, d_1(X_2, t)$,

$\overline{d^2(X_j, t)}$, $\overline{d_1^2(X_j, t)}$ = mean square values of $d(X_j, t)$ and $d_1(X_j, t)$, $j = 1, 2$.

It should be recalled, in general, that the absolute value of the cross-correlation coefficient is less than, or equal to, 1.0, and that the cross-correlation coefficient equals 1.0 when the value at a point is correlated to itself.

More significant than particular values of the cross-correlation coefficient is the area under the curve of cross-correlation coefficient versus axial spacing distance. This area is defined as the correlation length (normalized with respect to cylinder diameter, D), and is considered to be the measure of spatial correlation. It is given by

$$\chi_{k^2}(X_m) = \int_0^\infty R_{k^2}(X_m, \Delta X)\, d\left[\Delta X/D\right], \quad k = \ell, d$$

where

$X_m$ = axial coordinate of a fixed reference station

$X_n$ = axial coordinate of a relocatable station

$$\Delta X = \begin{cases} X_m - X_n \\ \quad \text{or} \\ X_n - X_m \end{cases}$$

Note: $\Delta X$ is defined such that $\chi_{k^2}$ is positive.

## 4.2 Model Shakedown and Referencing to Previous Results

In line with intentions that this study should extend the results of reference 11 and as a procedural check, some of the test points from the wind tunnel runs of Schmidt (11) were repeated. Aspects considered were verification of the fact that the statistics could be repeated; and

determination of any deviations due to changes in model surface finish, degree of cleanliness of the air in the wind tunnel (freedom from foreign particles), and other related factors. Comparison of the model as tested for the study presented here and as used to obtain data leading to findings of reference 11 revealed a smoother surface condition due to added hand-polishing with crocus cloth and kerosene. After each model change, the surface was inspected, hand-polished, and wiped with cleaning solution (aerosol-type Bon Ami). After each run the above procedure was repeated.

At this point it should be recalled that $X$ is the axial coordinate along the cylinder axis, and that $X = 0$ at the blunt-end. The origin of the X-axis is fixed in space regardless of the addition of the nose shapes or the shaker. The above-mentioned reruns (and the selected points from reference 11) are presented as curves of cross-correlation coefficient versus $\Delta X/D = (X_2 - X_1)/D$ for fixed $X_2/D = 3.239$ (Figures 13 and 14). The values of $R_{\ell 2}$ come close to corresponding values of reference 11. Even though only two test points per Reynolds number were taken, a curve was faired in order to obtain approximate values of the correlation length. Two additional points were available to facilitate curve drawing since the cross-correlation coefficient is unity at $\Delta X/D = 0$ and since, according to reference 11, the lift force cross-correlation coefficient is already very small at $\Delta X/D$ of about 2.4.

For Reynolds numbers of $1.53 \times 10^6$, $0.65 \times 10^6$ and $0.75 \times 10^6$ (i.e., wind tunnel dynamic pressure, $q = 20$, 30 and 40 psf, respectively) values of $\chi_{\ell 2}$ are about 0.55, 0.46 and 0.52. This compares with

values obtained by Schmidt (11) of 0.475, 0.568, and 0.592. This margin would be expected to be narrower if there were more test points to better define the fairing.

The values of $R_{d^2}$ for Reynolds numbers of $0.53 \times 10^6$ and $0.65 \times 10^6$ correspond to the results of reference 11 that have been given an apparent shift of $\Delta X/D = +1.6$. Results for $R_{d^2}$ at Reynolds number of $0.75 \times 10^6$ are consistent with the findings of Schmidt (11).

## 4.3 Unsteady Lift and Drag

In contrast to the work by Schmidt (11), whose axial reference location was Channel 2 fixed at $X_2/D = 3.239$, the datum level used in this study was Channel 1 fixed at $X_1/D = 0.523$. Channel 2 was initially adjacent to Channel 1 ( $\Delta X/D = 0.316$); $\Delta X$ was increased by moving Channel 2 down away from the tip.

During the wind tunnel tests for this study, it was noted that the root-mean-square (RMS) values of lift and drag for the conical tip installation were close to those of the smokestack configuration (Figures 15 to 18). Accordingly, the sequence of tests for the conical tip was abbreviated in order to devote greater wind tunnel time to a more complete investigation of loads near the tip of the smokestack. For the same reason, in view of the similarity in the results between ellipsoidal and hemispherical tips (Figures 19 to 21), the program for the ellipsoidal tip was curtailed.

In all cases the effect of the tip is evident. In general, the conical end and the smokestack show the lesser amount of load intensification

near the tip (See Figures 15 to 18): and the ellipsoidal and hemispherical ends cause a much larger increase in loads when the tip is approached (See Figures 19 to 21). Near the free end, unsteady lift for the ellipsoid starts higher and drops more rapidly than that for the hemisphere (See Figures 19 and 21). In the case of the ellipsoid, the unsteady lift starts about 20 per cent lower (at $X/D = 0.5$), peaks near $X/D = 0.8$, and then rapidly drops. Values of unsteady drag for the ellipsoid are around 20 per cent lower than values for the hemisphere in the region $0.5 < X/D < 0.8$. Influence of these two tip shapes is indiscernible for distances from the tip greater than about $X/D = 2.4$.

Compared to smokestack findings, the ellipsoidal and hemispherical tips cause significant increases in RMS values. For $X/D < 2.0$, the unsteady lift for these two shapes is two to three times that of corresponding values for the smokestack (See Figures 15, 19 and 21). For $X/D < 0.8$ unsteady drag for the two shapes is about twice that of comparable values for the smokestack (See Figures 16, 20 and 21).

Relative to the smokestack, use of the conical tip appears to attenuate the intensification of forces near the free end of the model (Figures 15 to 18). The two sets of data lie too close to draw definite condlusions. The scatter expected for random measurements of the type made is about the same order as the difference between the findings for the cone and smokestack. This dispersion is shown in Figures 22 and 23 for unsteady lift and drag for the smokestack and the hemisphere. The curves consist of fluctuating forces plotted versus dynamic pressure

(fixed $X_1/D = 0.523$) for five different data runs. Much of the spread can be attributed to slight variations in tunnel operating conditions, model surface quality, and to the fact that the loads phenomena are only locally stationary —— on the order of seconds.

As pointed out in Section 4.2, the model was hand-polished and wiped off, especially near the instrumented load-sensing sections, between every run. Inasmuch as loads are extremely sensative to model surface condition, it is not unreasonable to expect that such a continual smoothing process will influence unsteady lift and drag.

In hopes of obtaining a more complete picture of the loads near the free end of the model, values of the steady component of drag in this region were examined for the blunt-end and hemispherical configurations. Comparisons of a preliminary nature were made with the findings of Schmidt (11), but no conclusions could be drawn. It appeared that there was something less than a two-fold increase in steady drag near the model tip for the configurations noted over that for the blunt-end in the area, $X/D = 3.0$. In this vicinity, Schmidt obtained a coefficient of about 0.33 for the steady component of drag.

## 4.4 Axial Correlations near the Model Tip

To obtain an essential aspect of the description of the forces involved, plots of cross-correlation coefficients versus $\triangle X/D = (X_2 - X_1)/D$ for fixed $X_1/D = 0.523$ were made for the smokestack and the hemispherical tip (Figures 24 to 27). The curves, in theory, should be smooth; but there are not enough data to show the character of the curves. The dashed lines only show the succession of data points.

For both the blunt-end and the hemisphere, a jump in $R_{\ell 2}$ from a positive to a negative correlation is exhibited for $0.3 < X/D < 0.5$ (See Figures 24 and 26). This indicates, on the average, a large phase difference between load-sensing Channels 1 and 2. No connection can be justifiably made between these negative correlations and the high or increasing RMS values of lift coefficient (Figures 15 and 19). For the hemisphere, peak unsteady lift occurs at $X/D = 0.839$, which corresponds to $\triangle X/D = 0.316$. At $X/D = 1.039$, corresponding to $\triangle X/D = 0.516$, values of unsteady lift average only around 13 per cent less than peak values. Thus, large values of unsteady lift, similar in magnitude, occur at $X/D = 0.839$ and 1.039. But $R_{\ell 2}(\triangle X/D = 0.316) \simeq +0.65$ and $R_{\ell 2}(\triangle X/D = 0.516) \simeq -0.50$. It can only be concluded that separation phenomena on some large scale occurs for the approximate range, $0.6 < X/D < 1.2$ or $0.1 < \triangle X/D < 0.7$. The presence of the hemispherical end acts as an intensifying factor.

Intuitively, one might assume that the slender conical tip (2 diameters long) and ellipsoidal tip (1.5 diameters long) cause an effective shift of the load-sensing stations away from a fictitious free end. This appears to be substantiated by the unsteady lift plots for the ellipsoid and the hemisphere (See Figures 19 and 21). In the case of the ellipsoidal tip, RMS values are maximum for minimum X/D (for data obtained) and descent rapidly (Figure 21). This is apparently consistent with the hemisphere if one imposes a $-0.3$ shift of the X/D origin of the curve of RMS data for the hemispherical tip (See Figure 19).

As indicated by RMS values of lift for the smokestack and hemisphere (See Figures 15 and 19), the load intensification occurs not at measured regions closest to the tip. There is no immediate explanation for this. Added investigation is expected to clarify this; e.g., by power spectral analysis of available records and/or by future tests with measurements at more stations near the tip. Notwithstanding the negative values at $\Delta X/D = 0.516$, other points on the $R_{\ell 2}$ curve and points on the $R_{d^2}$ curve for the smokestack (fixed $X_1/D = 0.523$) lie quite close to the values of Schmidt (11) for fixed $X_2/D = 3.239$ (See Figures 13, 14, 24 and 25). This would lead one to conclude that, but for a localized intensity, the cross-correlation is much the same near the center of the model as near the model tip. Inasmuch as the correlation length (the area under the correlation curve) is considered the measure of spatial correlation, this possible conclusion cannot be evaluated until there are enough data to define a complete correlation curve.

## 4.5 Localized Boundary Layer Tripping

To facilitate a controlled disturbance near the tip of the smokestack in the form of localized boundary layer tripping, an air-blowing cylinder section was installed adjacent to the fixed-location Channel 1 ($X_1/D = 0.523$). The section, of length 0.7 of a cylinder diameter, had two 0.020 inch diameter orifices located at the $\theta = \pm 30$ degree positions and connected in parallel to a Fischer and Porter flow meter. Blowing was done out of one side of the cylinder only since symmetrical flow could not be assured. Flow meter

readings beyond a certain value were unreliable. Since at a certain flow the orifice is theoretically choked, any greater corresponding pressure indicates leaks in the hose and piping system. In general, blowing from one side induced a lateral force in the opposite direction. Figures 28 to 31 summarize the effects of blowing on lift for the four Reynolds numbers used in the tests.

At $Re = 0.38 \times 10^6$ and $0.53 \times 10^6$ ($q = 10$ and 20 psf) no effect was noted for the orifice volume flow rates used (See Figures 30 and 31). Significant changes in both steady and unsteady values of lift occured at $Re = 0.65 \times 10^6$ and $0.75 \times 10^6$ ($q = 30$ and 40 psf) (See Figures 28 and 29). To initiate a change in mean and RMS lift it took about seven times the orifice volume flow rate needed by Schmidt in his investigations (See Ref. 11). This, as in the cases of the various tip shapes, indicates the complexity of the separation phenomena in the vicinity of the tip.

## 4.6 Shaking of Cylinder with Smokestack

To ascertain if the motion of the cylinder affects the unsteady air loads, a shaker was installed on the blunt-end cylinder (See Figure 5). No significant change, with introduction of a periodic shaking force, was observed in correlation coefficients (Figure 32) or RMS values of lift (Figure 33). The unsteady lift values correspond to shaking frequencies of from 9.7 cps (cylinder fundamental frequency) to 53.9 cps.

Power spectral analysis of the model shaking data is a remaining area to investigate regarding effects of a periodic shaking force on unsteady air loads.

## V. CONCLUDING REMARKS

Need has existed for a systematic approach to the treatment of end effects, and the corresponding axial correlations, for a cantilevered circular cylinder normal to an air flow. Measurements have been made in the GALCIT Ten-Foot Wind Tunnel at Reynolds numbers (based on cylinder diameter) of $0.38 \times 10^6$, $0.53 \times 10^6$, $0.65 \times 10^6$ and $0.75 \times 10^6$ (corresponding to wind tunnel dynamic pressures of 10, 20, 30, and 40 psf, respectively).

It has been observed that the unsteady loads intensify near the cylinder model tip. This intensification is attenuated or enhanced depending on the tip configuration. For example, near the tip, the unsteady lift for the hemispherical and ellipsoidal tips in two to three times the corresponding values for the smokestack. The conical tip yields RMS lift that is somewhat less than the lift of the blunt-end cylinder.

Besides variation in tip configuration, localized boundary layer tripping can be considered as a controlled disturbance at the free end of the model. Significant changes in mean and RMS lift were not found at Reynolds numbers less than $0.75 \times 10^6$. To get sizable changes in steady and unsteady values of lift, it required an orifice mass flow rate of about seven times that needed by Schmidt in his studies (11).

In contrast to the air blowing, shaking of the model, even at its resonant frequency of 9.7 cps, did not result in sizable changes in RMS lift or cross-correlation coefficient. It remains for a power spectral analysis to complete the picture.

In light of the initial investigations made during this study and the conclusions stated above, possible directions of future work can be outlined. Tests are needed to obtain data to fill in gaps or to complete records of information treated in this report. Most of the graphical data included herein could well have additional points to better define the curves. By a simple redesign of the presently separate blunt-end cylinder top and end cap into an integral unit, data can be obtained at an axial distance from the end of 0.367 cylinder diameters. This compares with the axial distance of 0.523 diameters, currently the closest point to the smokestack tip at which forces can be measured.

To increase the reliability of the air blowing results, a redesign of that system is in order. Better sealing and greater durability of the hose and piping system will assure accuracy of results for higher mass flow rates. An independent metering and piping system for respective orifices at the $\theta = \pm 30$ degree locations will assure symmetrical flow out of the cylinder and enable investigation of the blowing phenomena when applied near the tip.

These modifications in equipment will result in learning further information that will hopefully lead to a breakthrough in understanding the problem of unsteady loads on a cantilevered cylinder and the related response problem.

## VI. REFERENCES


1. Goldstein, S.: "Modern Developments in Fluid Dynamics". Vols. I and II, Oxford University Press (1938).

2. Humphreys, J. S.: "On a Circular Cylinder in a Steady Wind". Ph.D. Thesis, Harvard University (1959).

3. Fung, Y. C.: "Fluctuating Lift and Drag Acting on a Cylinder in a Flow at Supercritical Reynolds Numbers". Technical Report EM 8-5, Space Technology Laboratories, Inc. (May 1958). Note: Shorter version published in: Journal of the Aerospace Sciences, Vol. 27, No. 11, pp. 801-14 (1960).

4. Fung, Y. C.: "The Fluctuating Lift Force Acting on a Cylinder Subjected to Forced Oscillations Perpendicular to a Flow at High Reynolds Numbers". Technical Report EM 8-19, Space Technology Laboratories, Inc. (September 1958). Note: Shorter version published in: Journal of the Aerospace Sciences, Vol. 27, No. 11, pp. 801-14 (1960).

5. Fung, Y. C.: "The Analysis of Wind-Induced Oscillations of Large and Tall Cylindrical Structures". Technical Report EM 10-3, Space Technology Laboratories, Inc. (June 1960).

6. Macovsky, M. S.: "Vortex Induced Vibration Studies". David Taylor Model Basin Report 1190 (1958).

7. Keefe, R. T.: "An Investigation of the Fluctuating Forces Acting on a Stationary Cylinder in a Subsonic Stream and of the Associated Sound Field". University of Toronto, UTIA Report 76 (1961).

8. Gerrard, J. H.: "1958 Measurements of the Fluctuating Pressure on the Surface of a Circular Cylinder. Part I. Cylinder of 1 in. Diameter". Aeronautical Research Council Report 19, 844.

9. Gerrard, J. H.: "An Experimental Investigation of the Oscillating Lift and Drag of a Circular Cylinder Shedding Turbulent Vortices". Journal of Fluid Mechanics, Vol. II, Part 2, pp. 244-56 (1961).

10. Delaney, N. K., and Sorensen, N. E.: "Low Speed Drag of Cylinders of Various Shapes". NACA TN 3038 (1953).

11. Schmidt, L. V.: "Measurements of Fluctuating Air Loads on a Circular Cylinder". Ph.D. Thesis, California Institute of Technology (1963).

12. Ezra, A. A., and Birnbaum, S.: "Design Criteria for Space Vehicles to Resist Wind Induced Oscillations". American Rocket Society, Paper No. 1081 - 60 (April 1960).

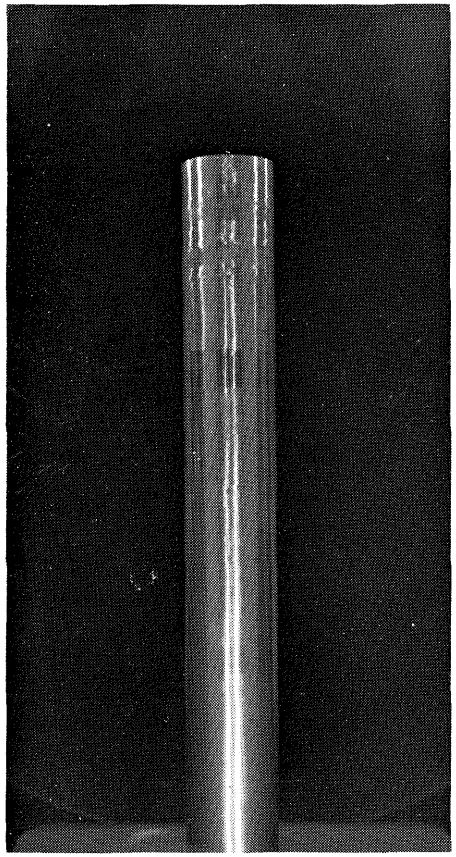

Figure 1 Cylinder Model in Smokestack Configuration

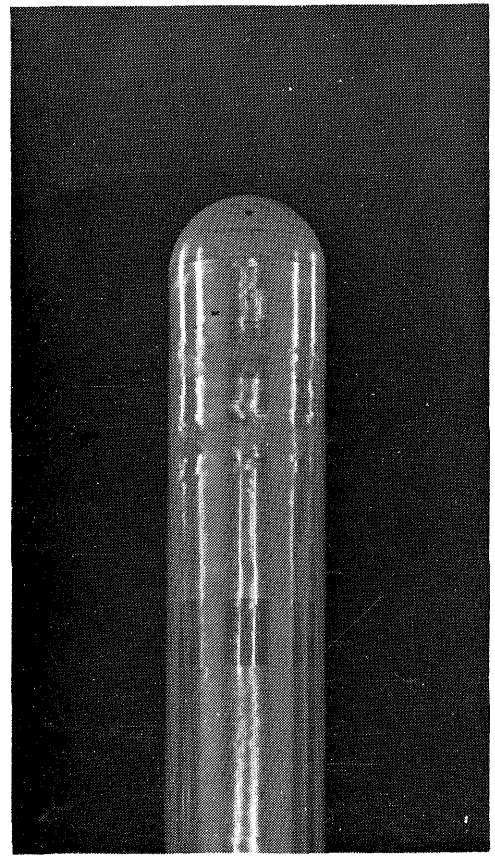

Figure 2 Model with Hemispherical Tip

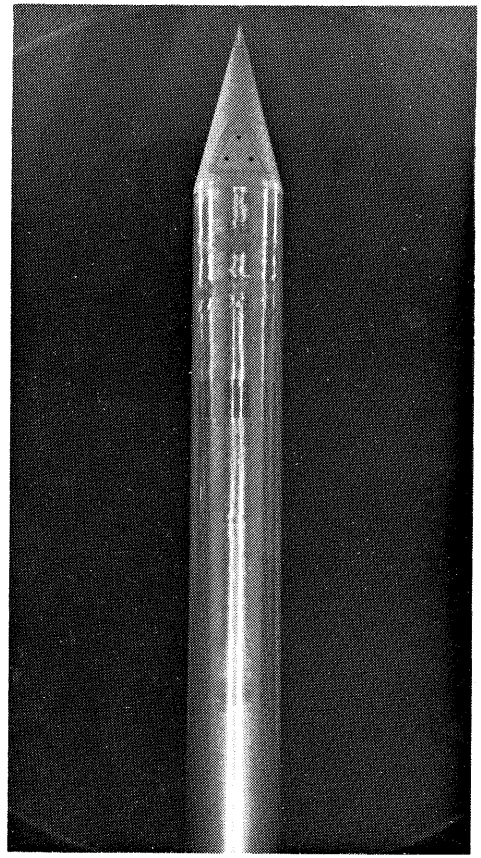

Figure 3 Model with Conical Tip

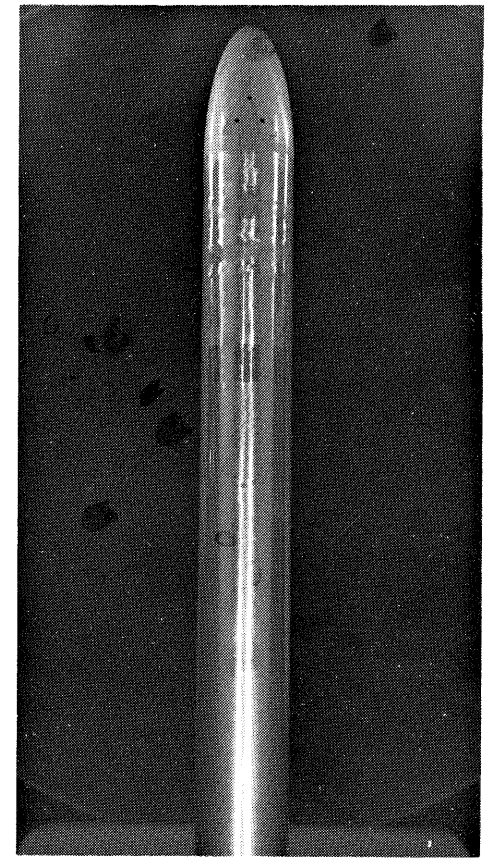

Figure 4 Model with Ellipsoidal Tip

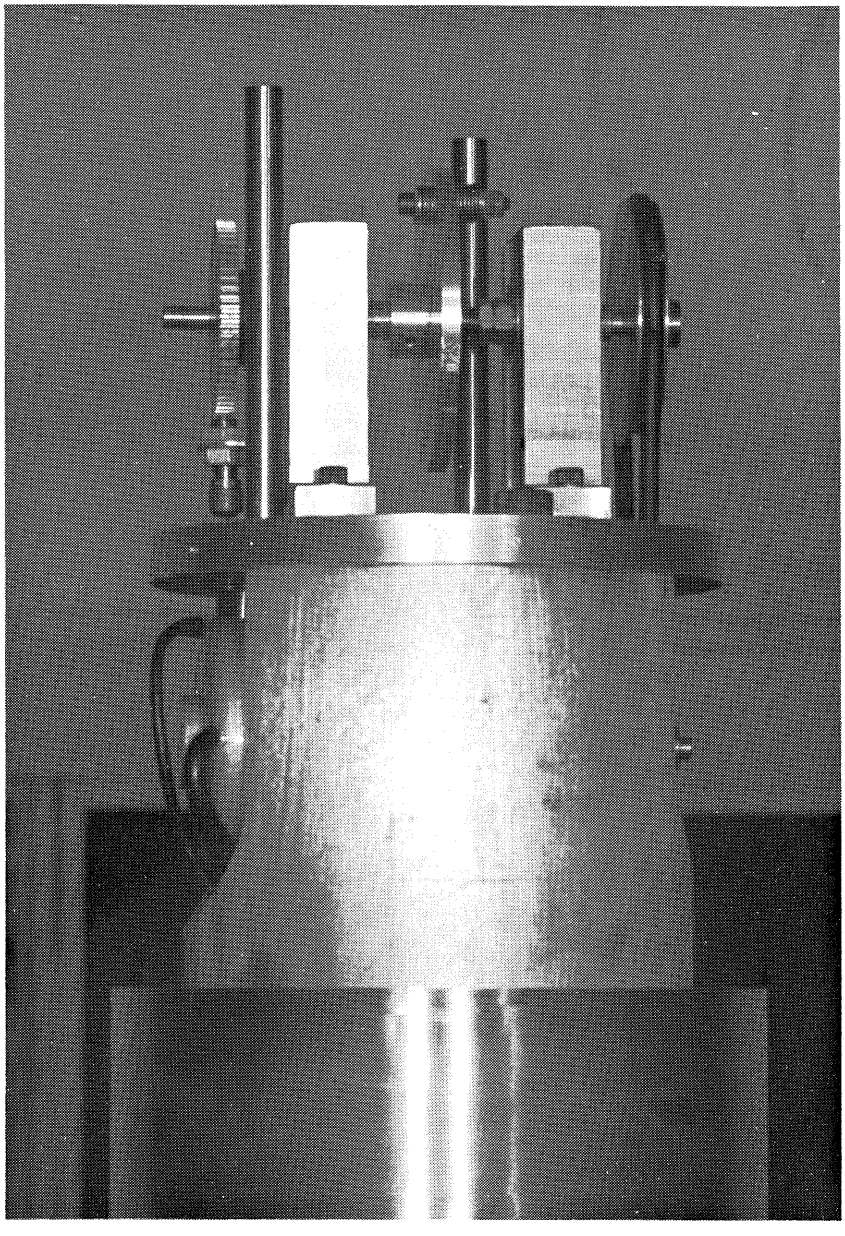

Figure 5 Model with Internal Shaker (Cylindrical Cover and Lid Removed )

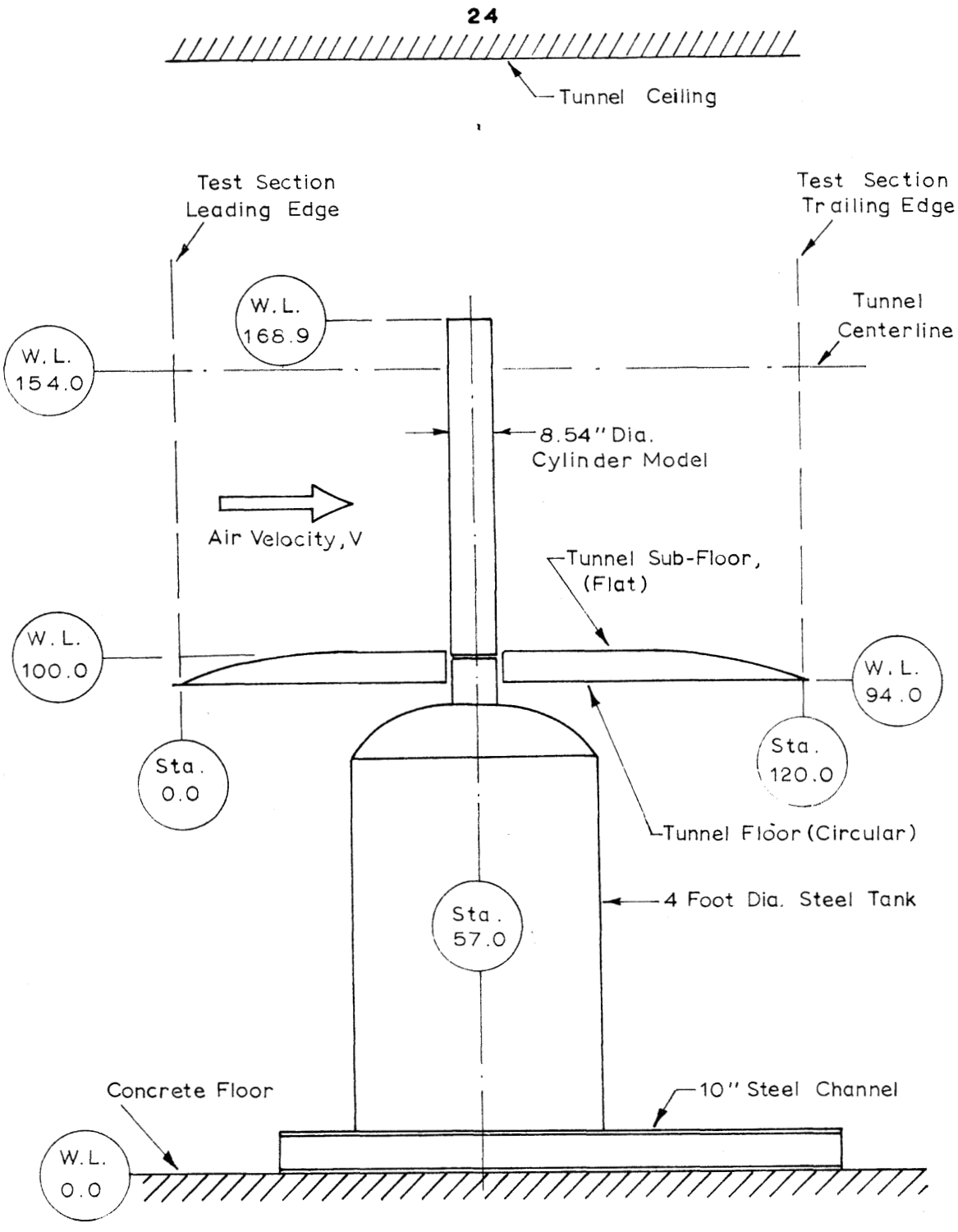


Figure 6 Model Installation in GALCIT Ten-Foot Wind Tunnel

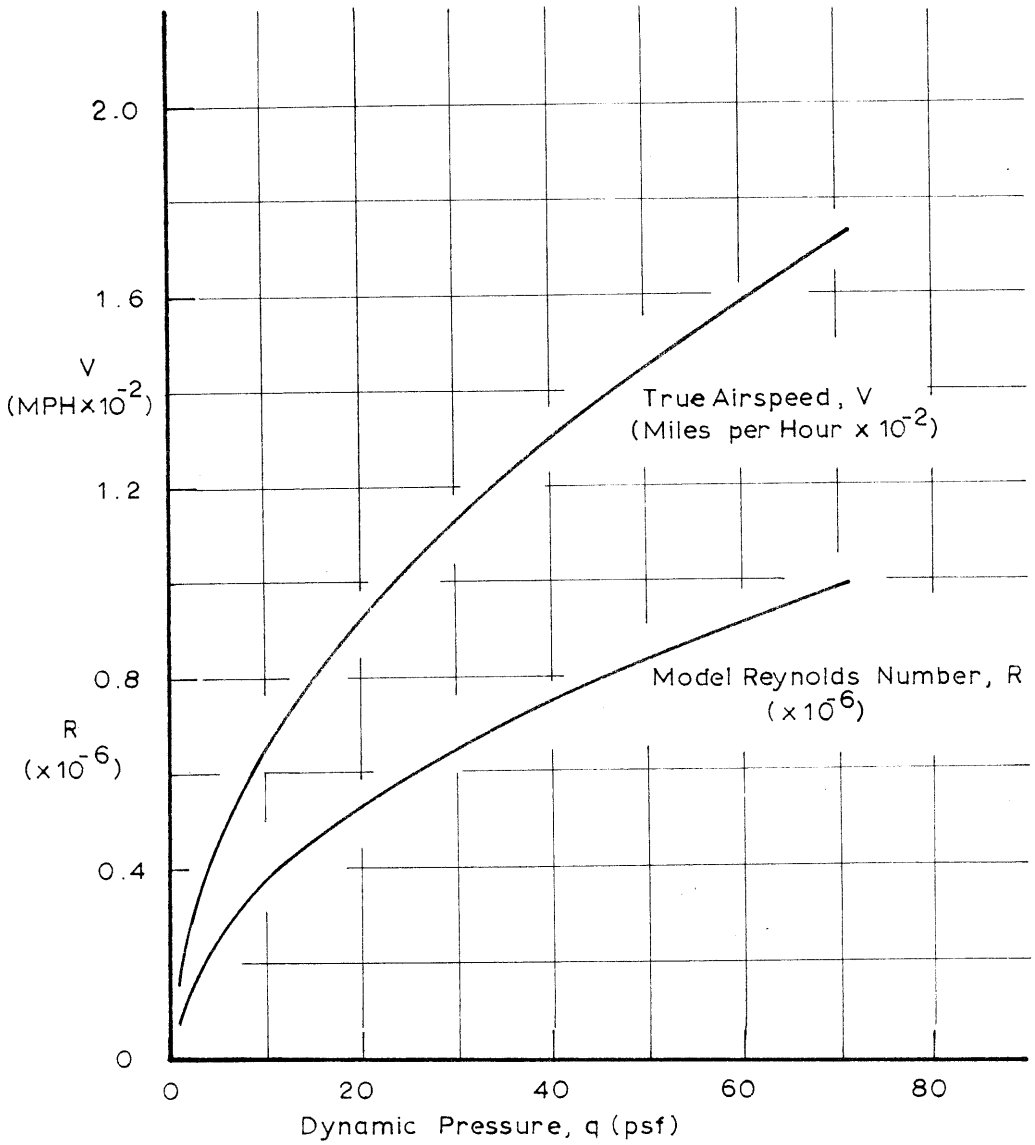


Figure 7 Average Tunnel Operating Characteristics

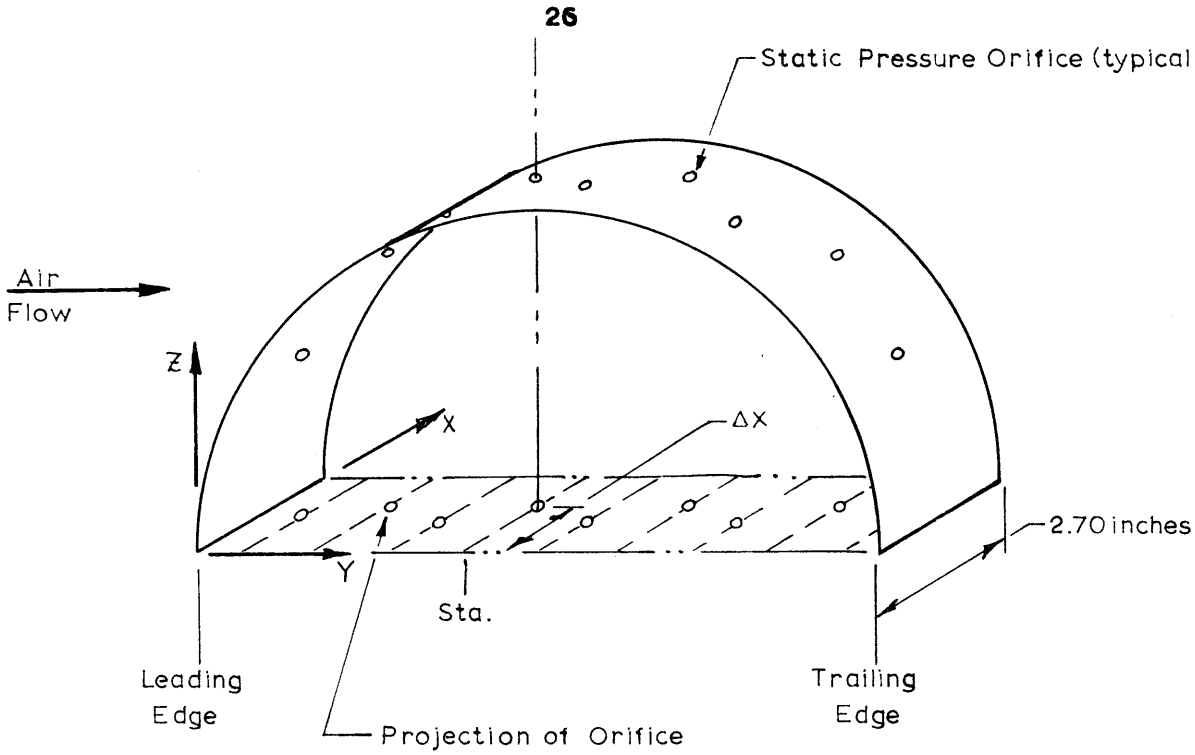


| Station | Y/D | ΔX (inches) | Δ R (inches) |
|---|---|---|---|
| 1 | 0.056 | 1.55 | 0 |
| 2 | 0.167 | 1.24 | -0.20 |
| 3 | 0.278 | 1.35 | +0.20 |
| 4 | 0.389 | 1.74 | -0.20 |
| 5 | 0.500 | 1.35 | +0.20 |
| 6 | 0.611 | 1.74 | -0.20 |
| 7 | 0.722 | 1.35 | +0.20 |
| 8 | 0.833 | 1.74 | -0.20 |
| 9 | 0.944 | 1.55 | 0 |

Note: 1. Cylinder Diameter = D = 8.54 inches
2. ΔR = Relative Displacement (X-direction) of the Orifice with respect to Pressure Transducer Centerline
3. Only One Side of Instrumentation Sector Shown for sake of clarity.
4. Orientation Corresponds to Lift Mode.

Figure 8 Pressure Orifice Orientation

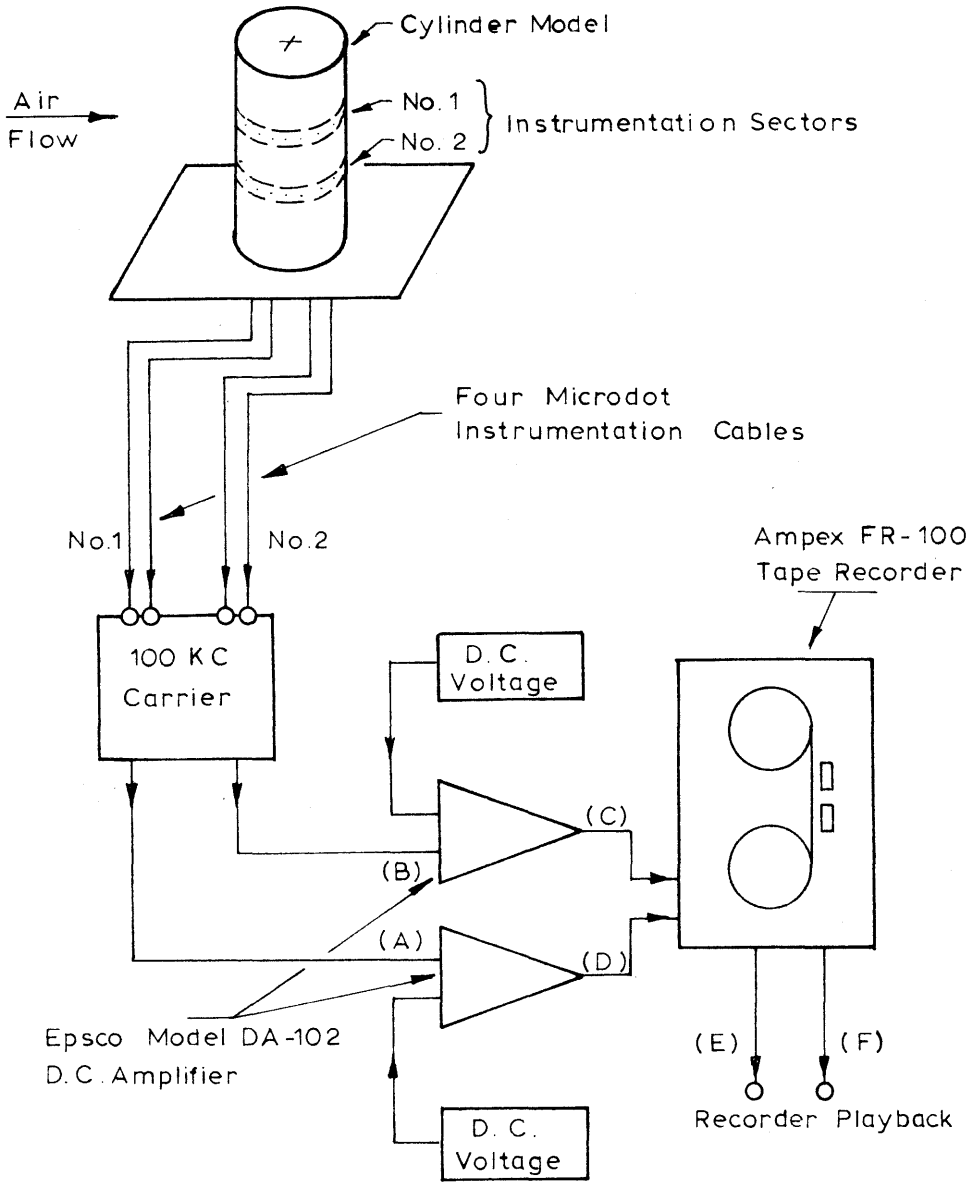


Note: Monitored Test Points are shown by (X)

Switch Panel Monitoring done by :

1. Ballantine Model 320 True RMS Voltmeter
2. Brown D.C. Voltmeter
3. Dumont Model 411 C.RO.

Figure 9 Schematic of Data Recording Circuitry

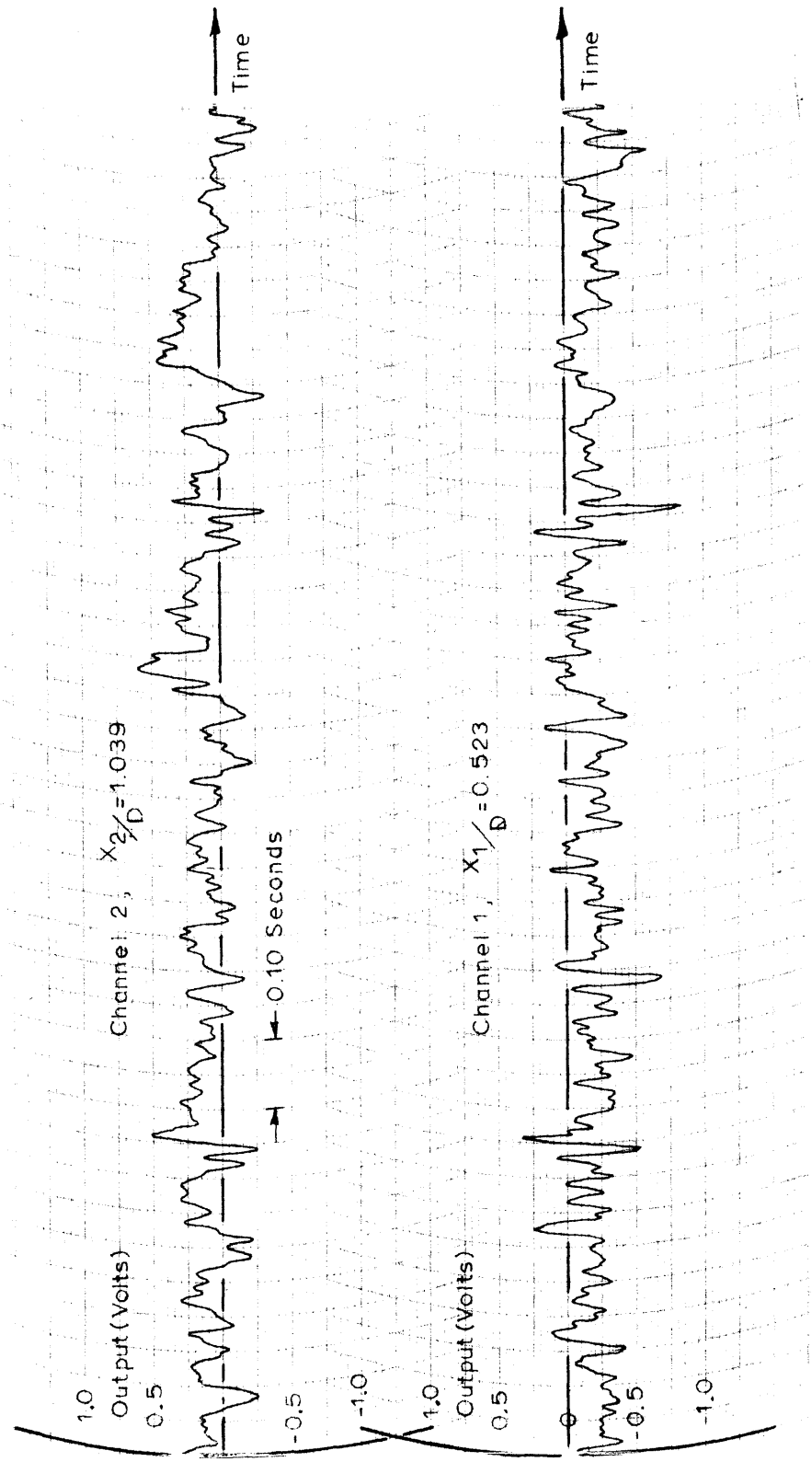


Figure 10 Typical Time Trace of Lift Forces Acting on the Smokestack

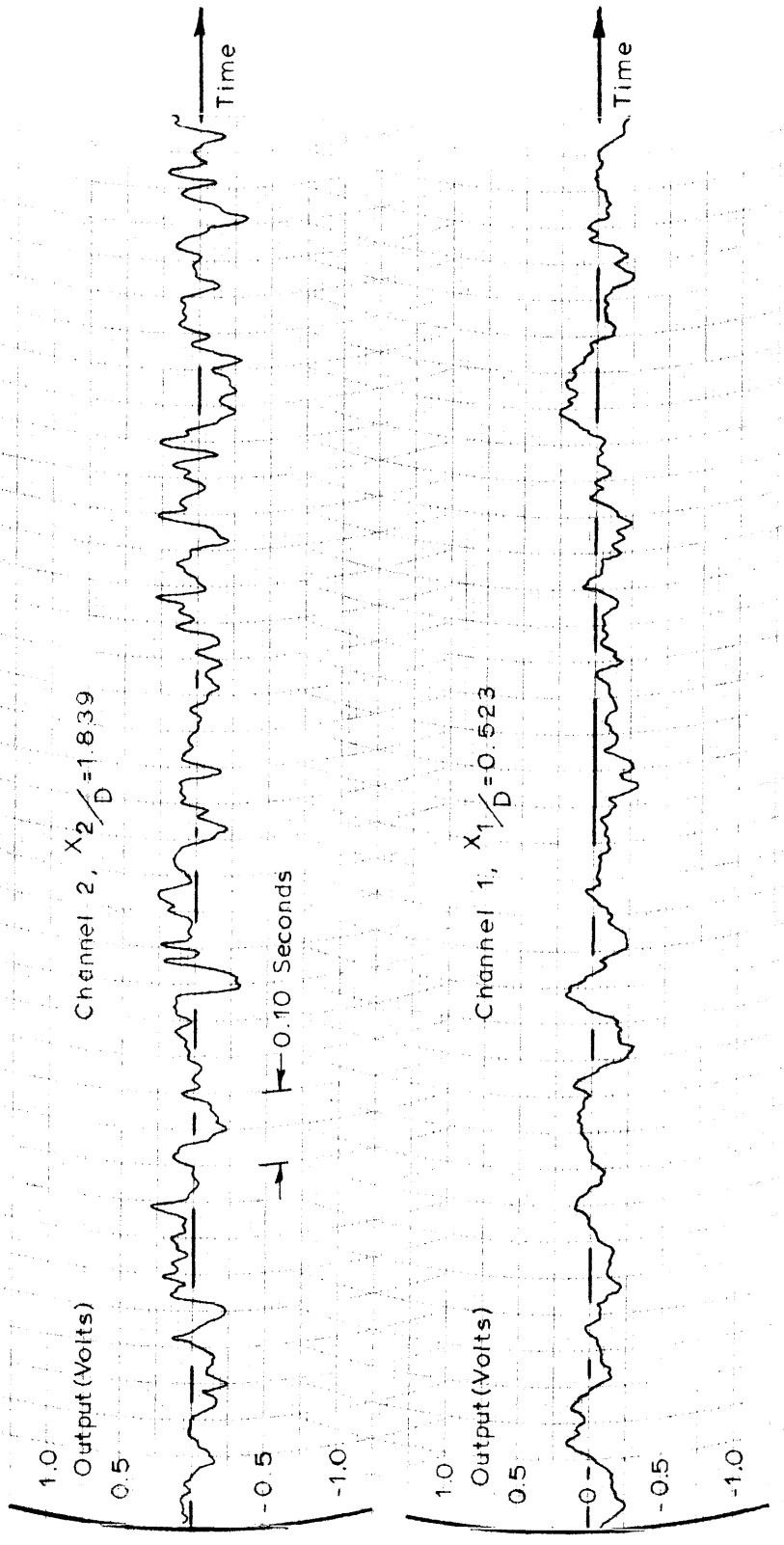


Figure 11 Typical Time Trace of Lift Forces Acting on the Model with an Hemispherical Tip

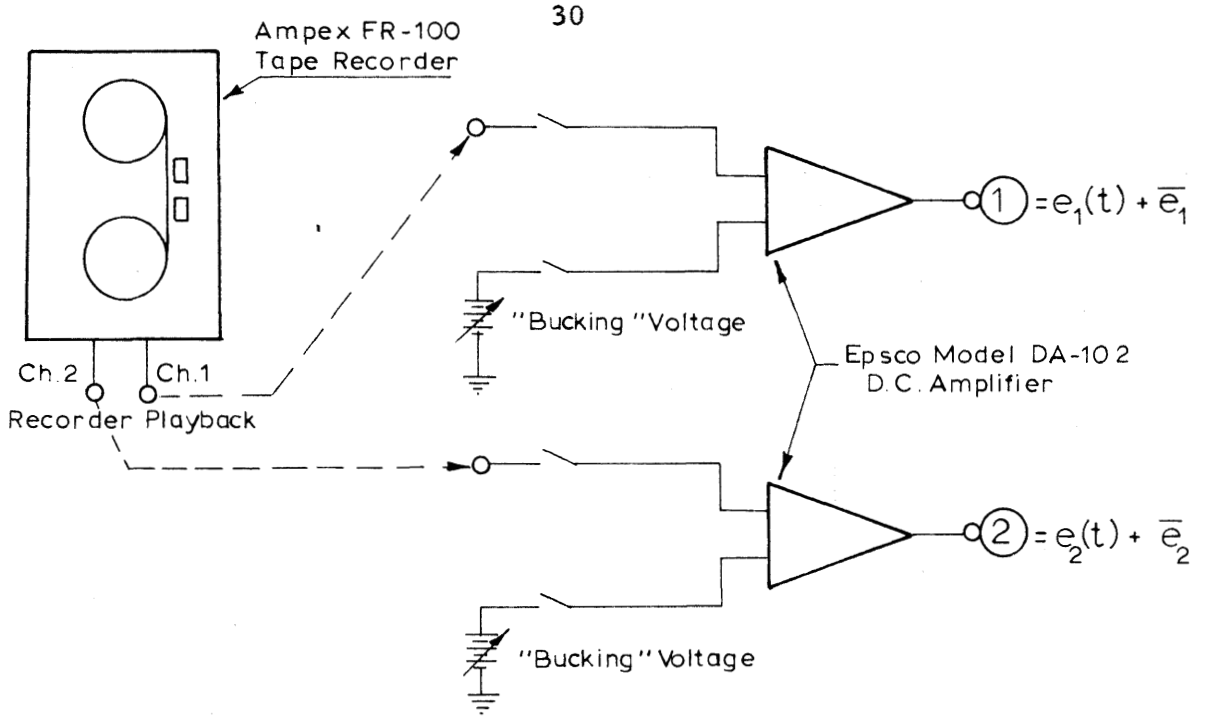


A. Amplifying Circuits

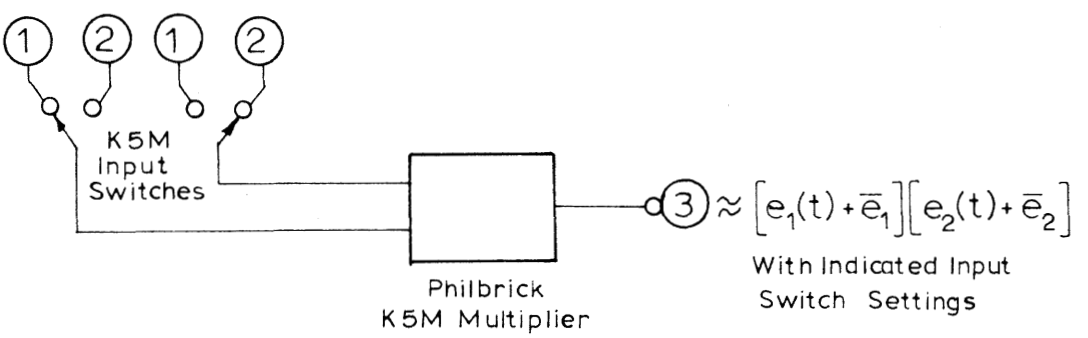


B. Multiplying Circuits

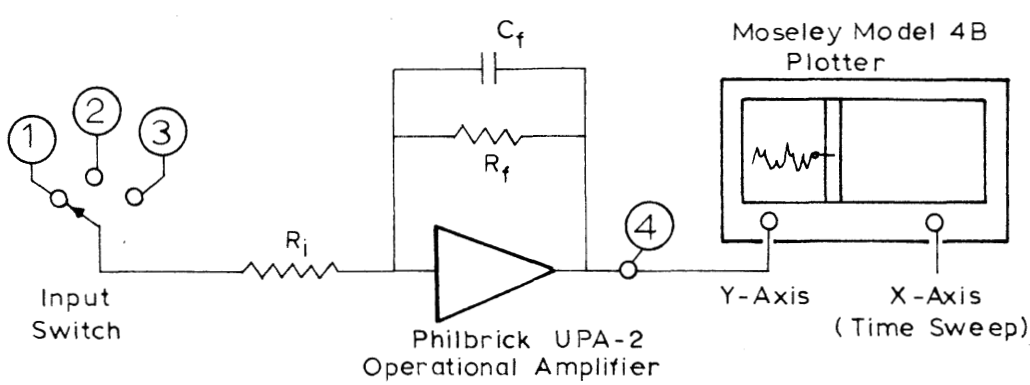


Switch at (1) $e_4 \approx \bar{e}_1$

" " (2) $e_4 \approx \bar{e}_2$

" " (3) $e_4 \approx \bar{e}_1\bar{e}_2 + \bar{e}_1\bar{e}_2$ (For Sample Case)

C. Time Averaging Circuit

Figure 12 Schematic of Analog Circuitry

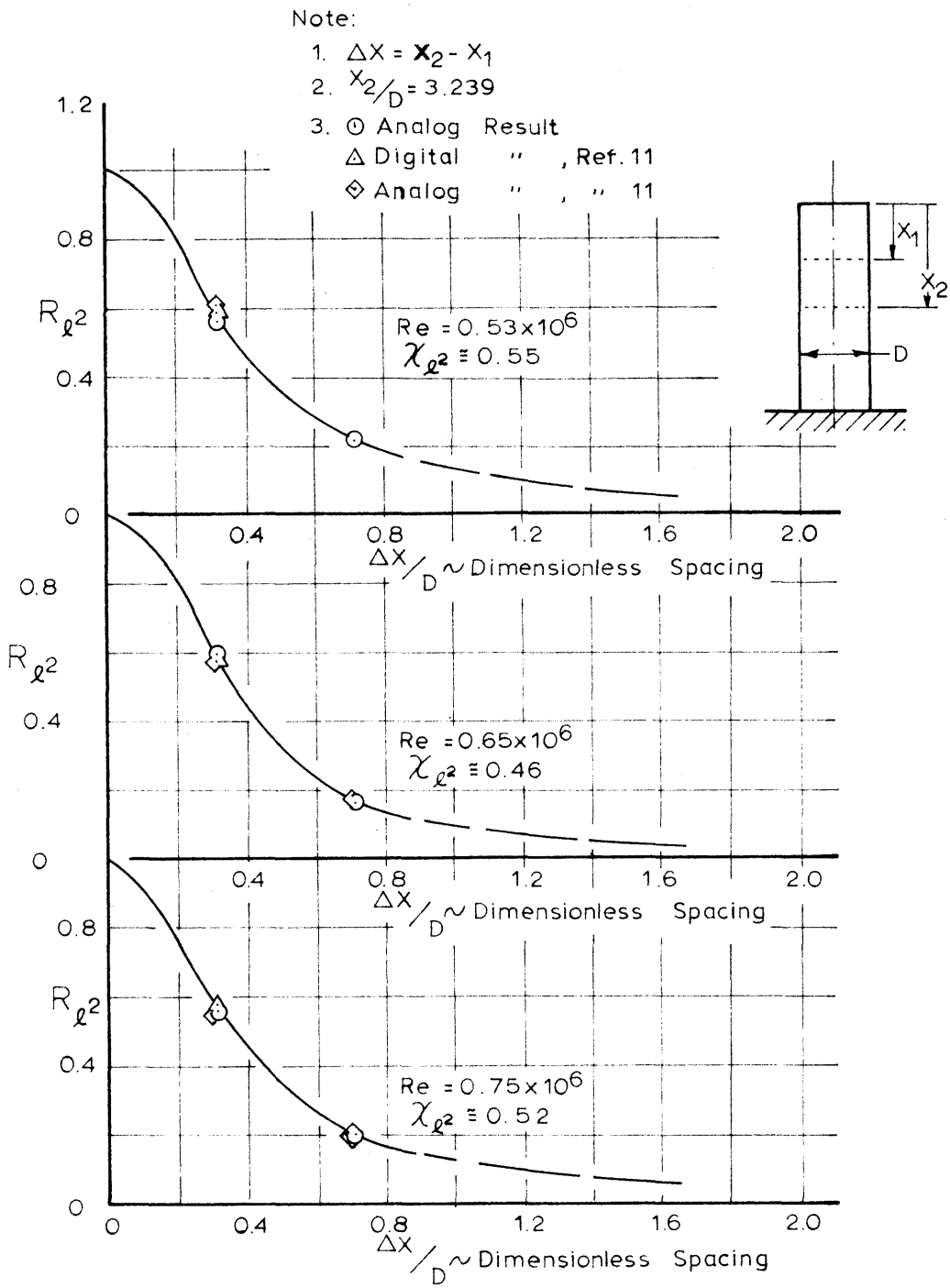


Figure 13 Lift Correlation for the Smokestack, $X_{2/D} = 3.239$

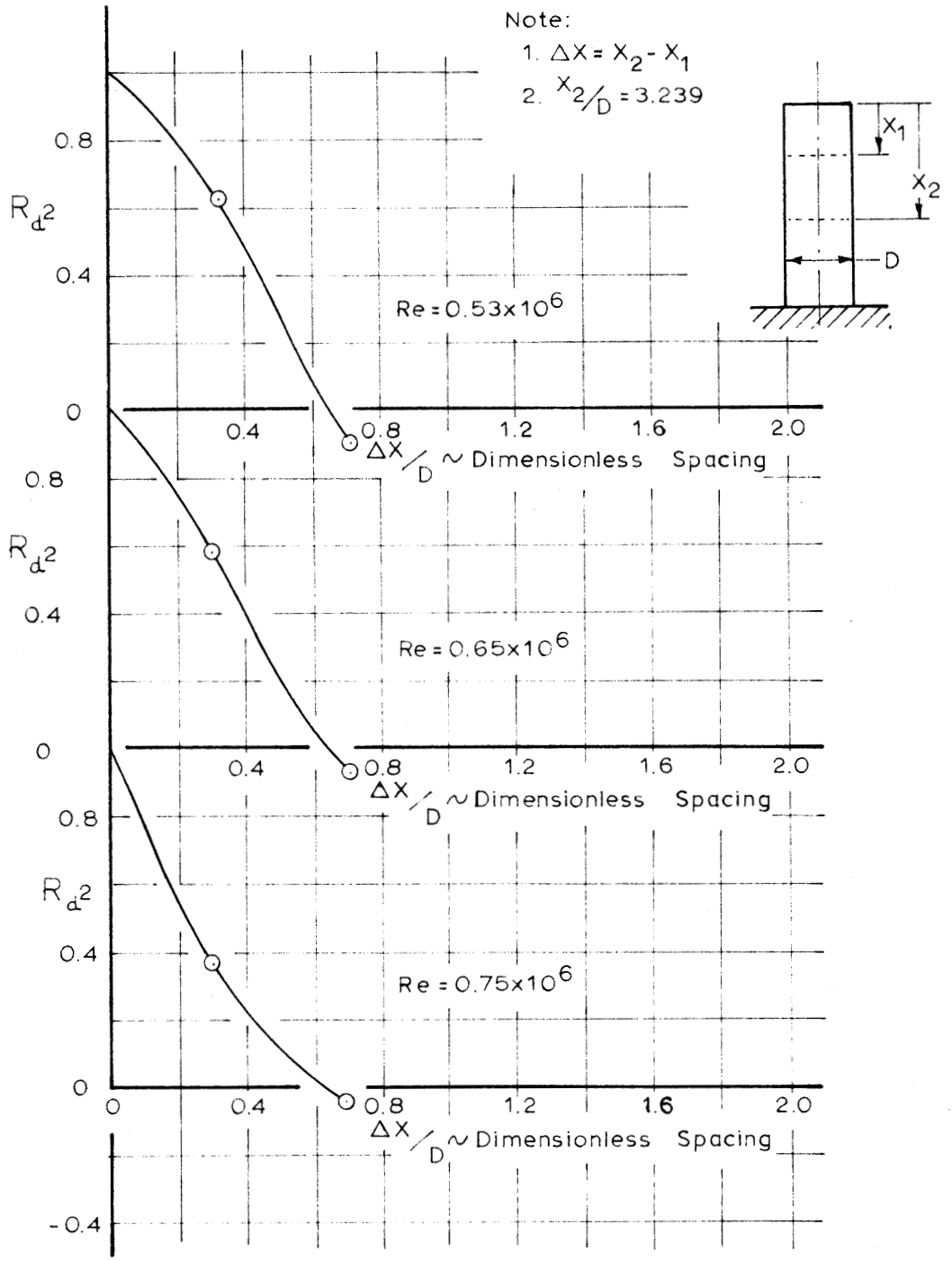


Figure 14 Drag Correlation for the Smokestack, $X_2/D = 3.239$

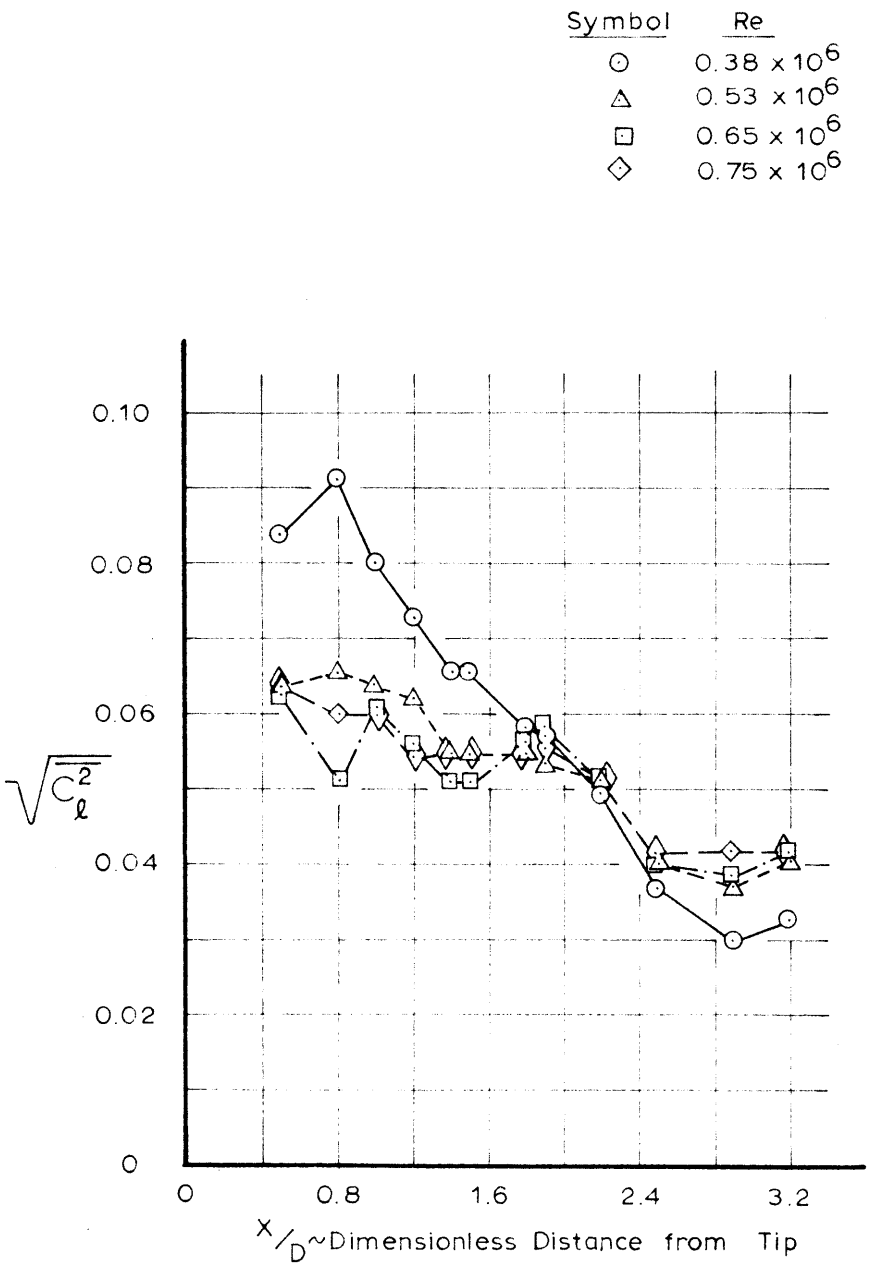


Figure 15 Unsteady Lift for the Smokestack

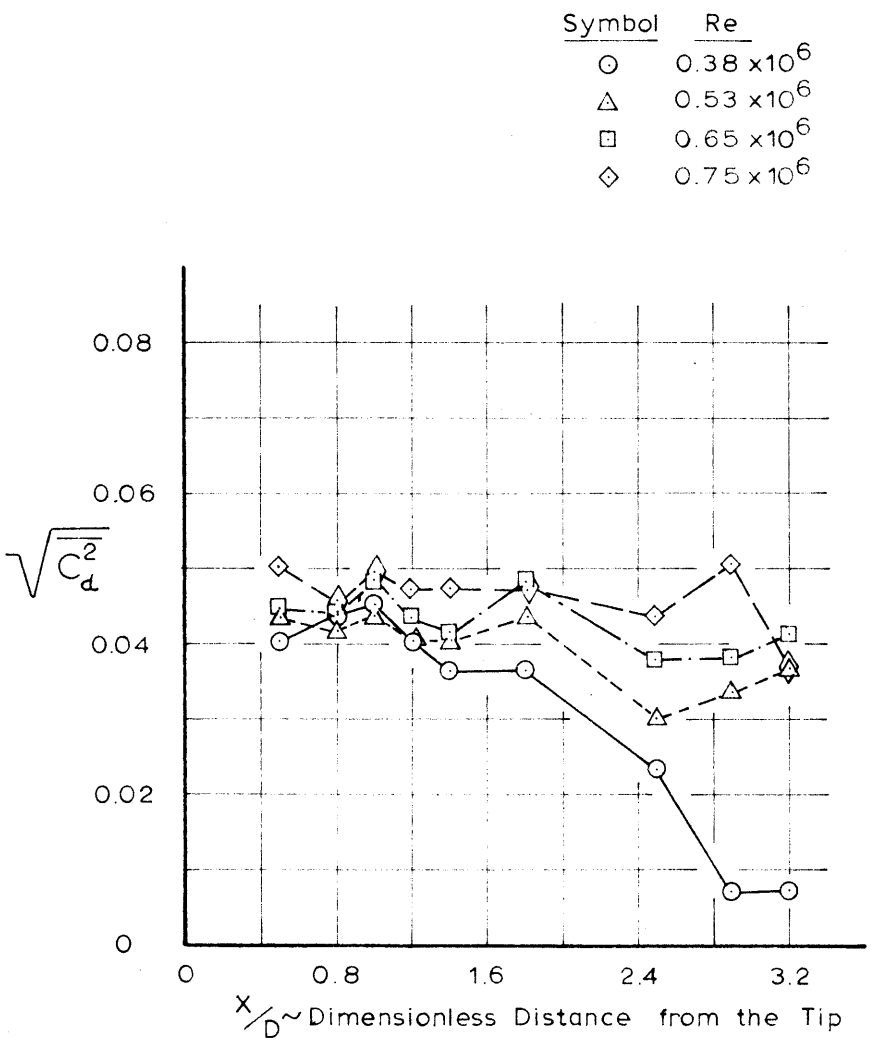


Figure 16 Unsteady Drag for the Smokestack

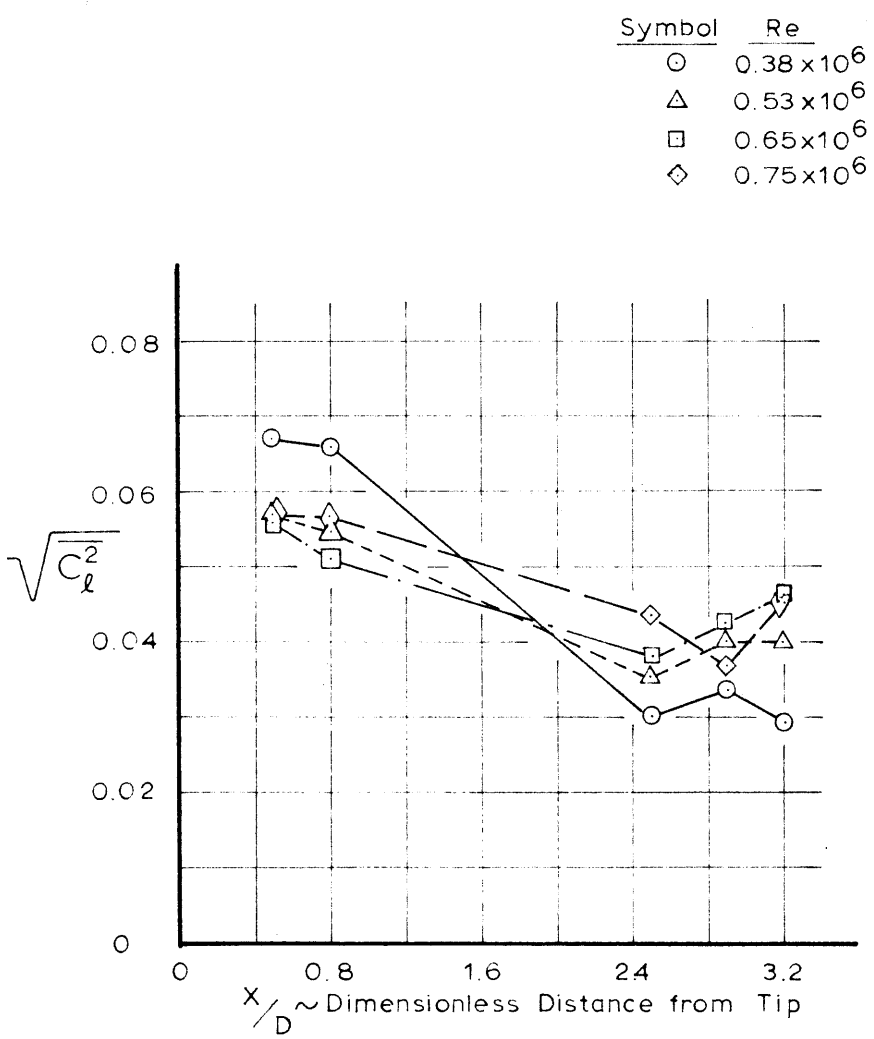


Figure 17 Unsteady Lift for the Conical Tip

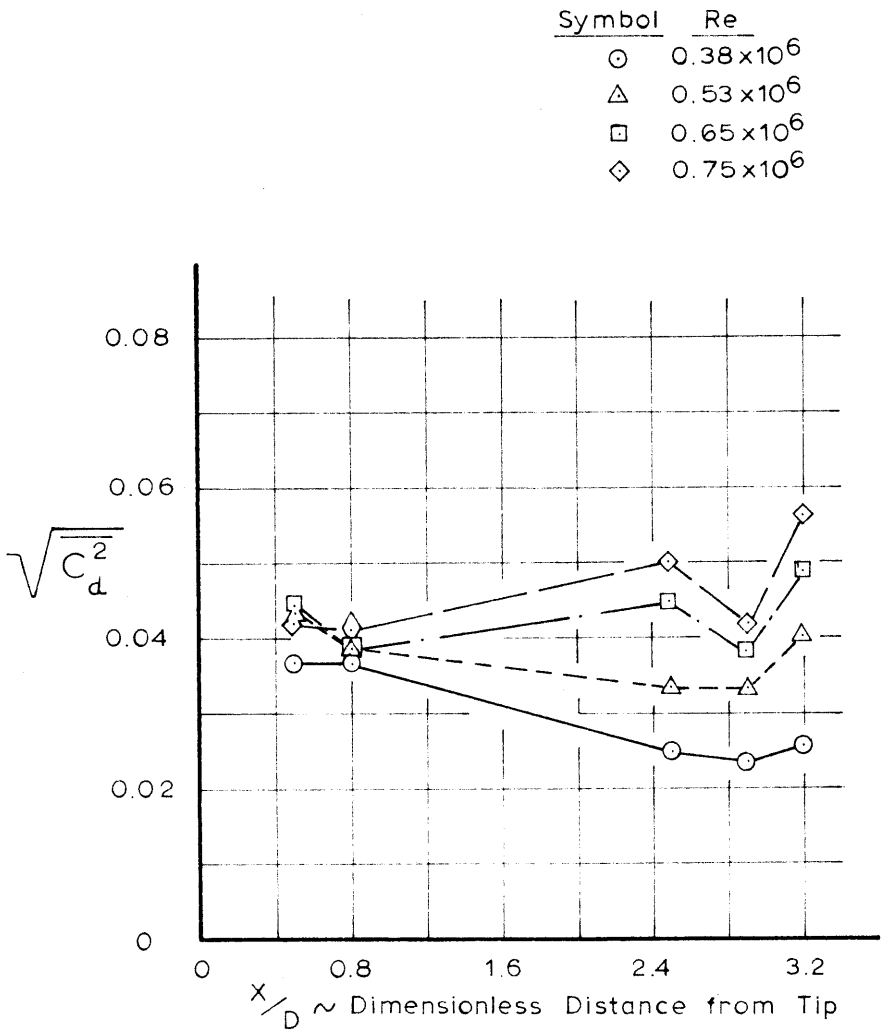


Figure 18 Unsteady Drag for the Conical Tip

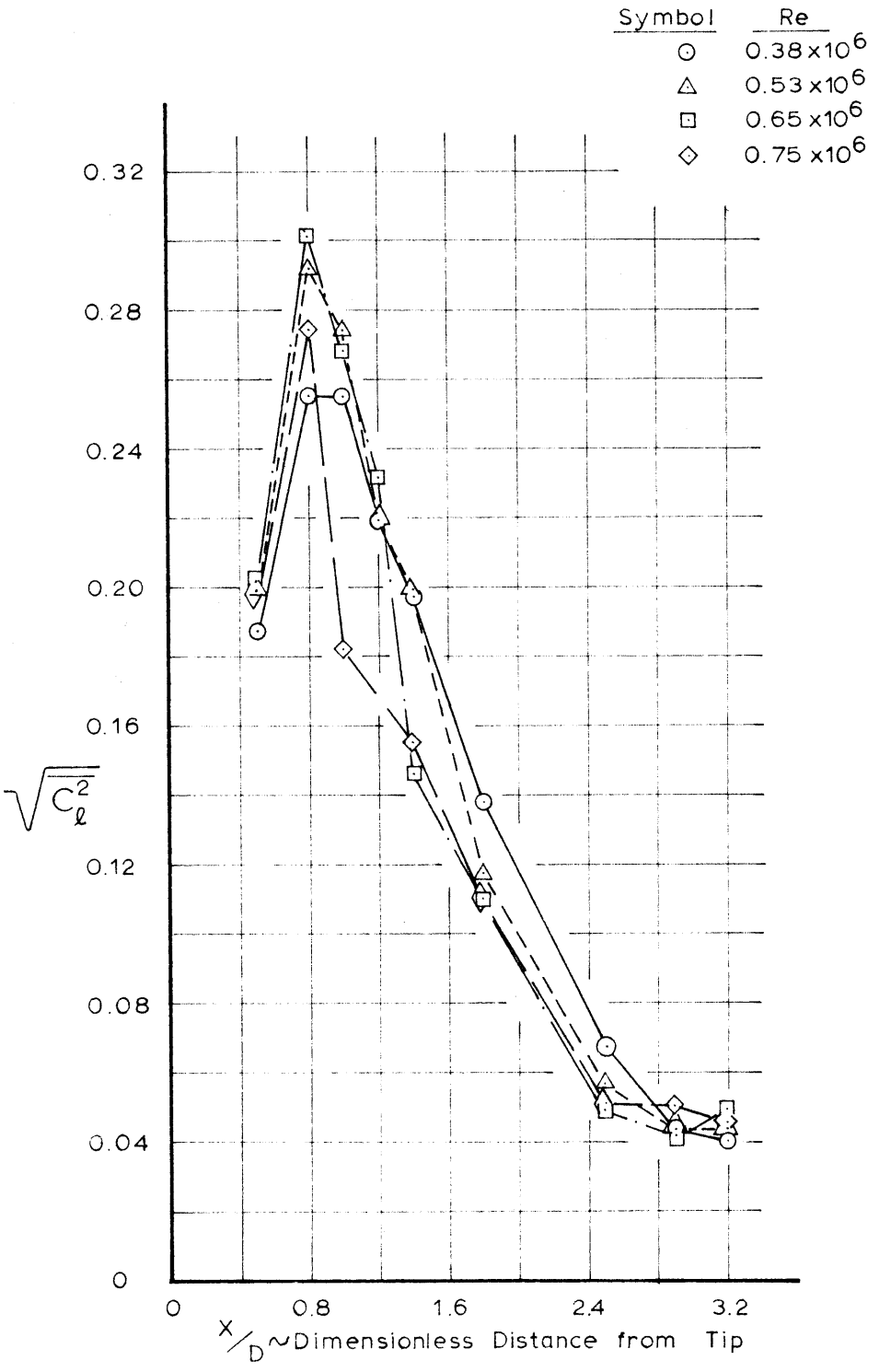


Figure 19 Unsteady Lift for the Hemispherical Tip

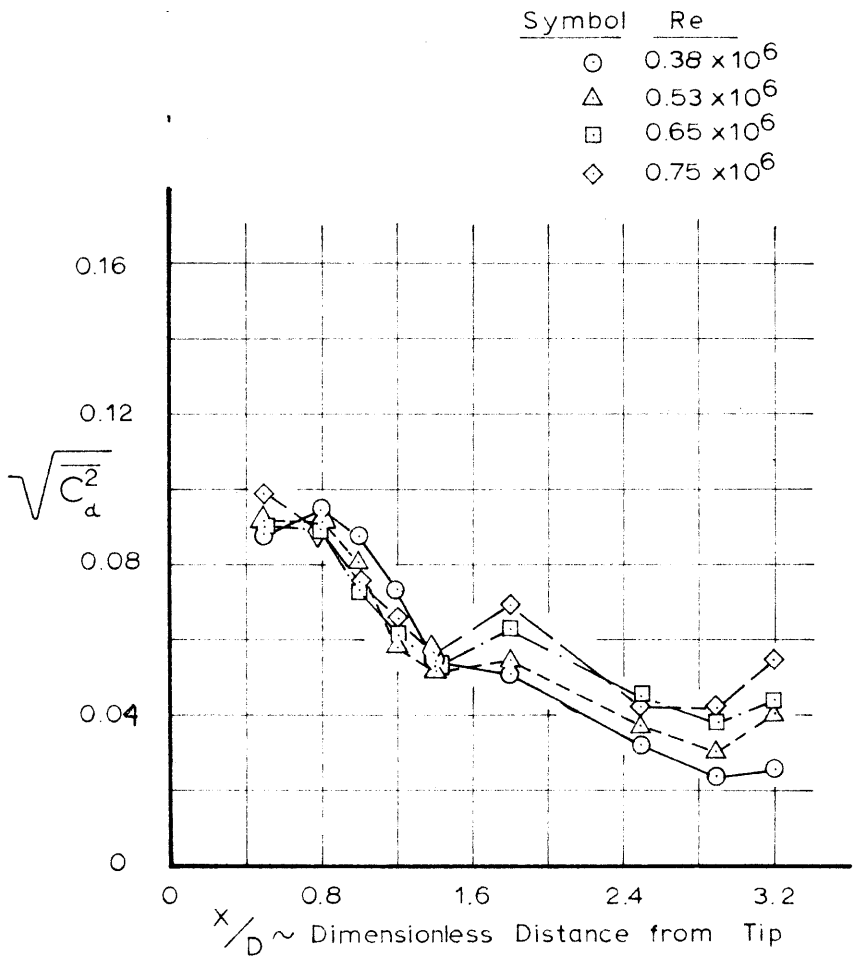


Figure 20 Unsteady Drag for the Hemispherical Tip

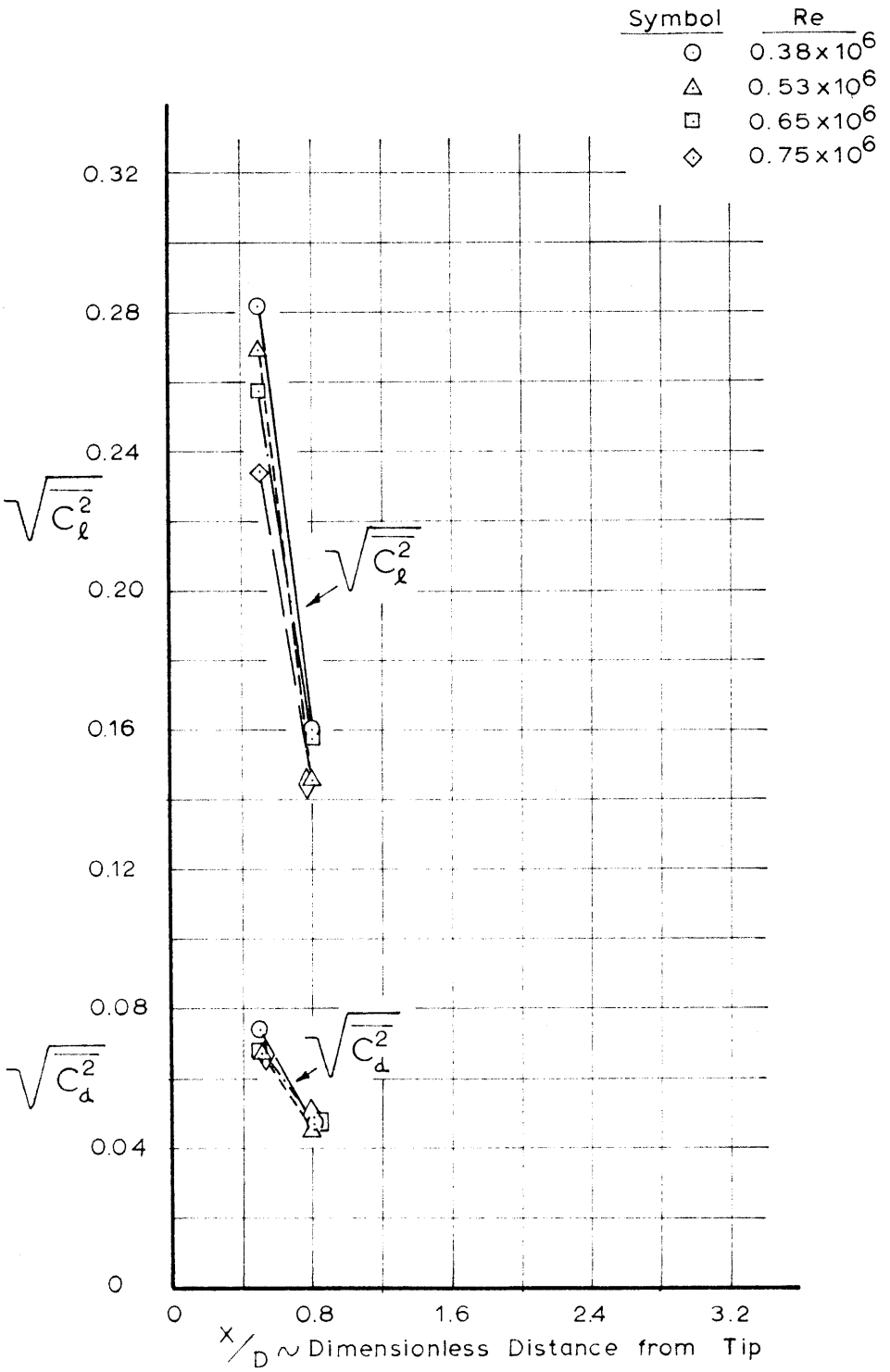


Figure 21 Unsteady Lift and Drag for the Ellipsoidal Tip

Note:
1. Data Apply to Channel 1 Load Station
2. Distance from Tip, $X_{1/D}=0.523$

| Symbol | Run No. $\sqrt{\overline{C_\ell^2}}$ | $\sqrt{\overline{C_d^2}}$ |
|---|---|---|
| ⊙ | 113 D | 120 |
| △ | 123 | 124 |
| ⊡ | 127 | 128 |
| ◇ | 131 | 132 |
| ▽ | 135 | 136 |

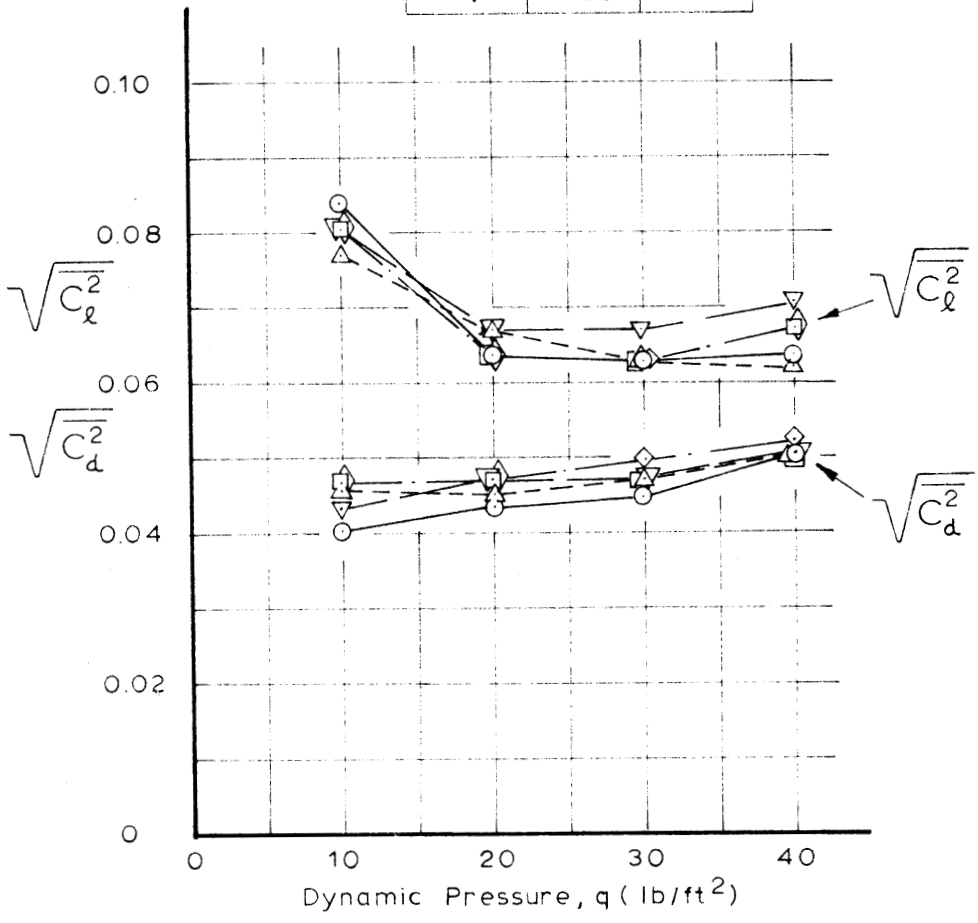


Figure 22 Unsteady Lift and Drag Summary, Smokestack Tip, $X_{1/D}=0.523$

Note:

1. Data Apply to Channel 1 Load Station
2. Distance from Tip, $X_1/D = 0.523$

| Symbol | Run No. $\sqrt{\overline{C_\ell^2}}$ | Run No. $\sqrt{\overline{C_d^2}}$ |
|---|---|---|
| ⊙ | 115B | 118 |
| △ | 126 | 125 |
| ⊡ | 130 | 129 |
| ◇ | 134 | 133 |
| ▽ | 138 | 137 |

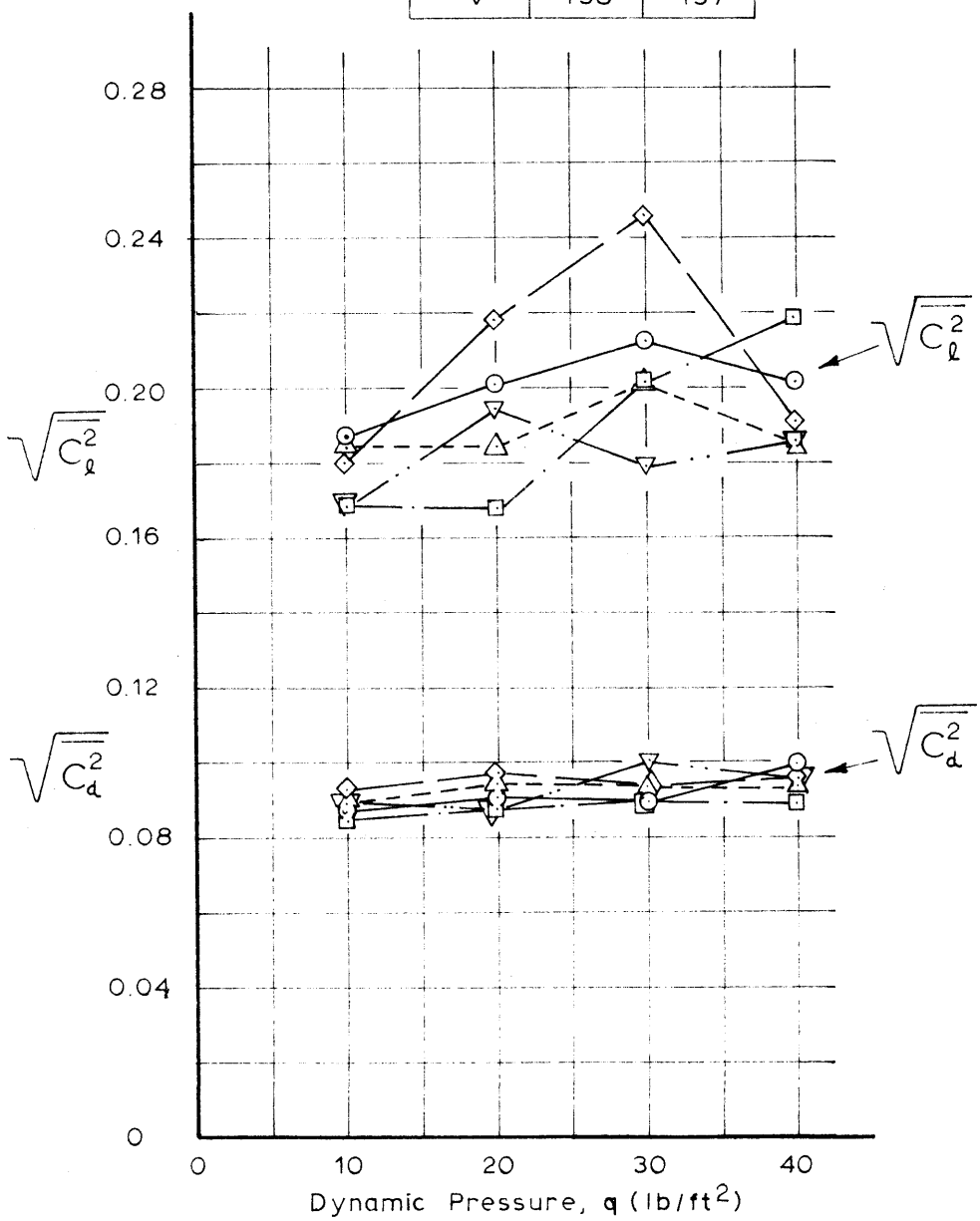


Figure 23 Unsteady Lift and Drag Summary, Hemispherical Tip, $X_1/D = 0.523$

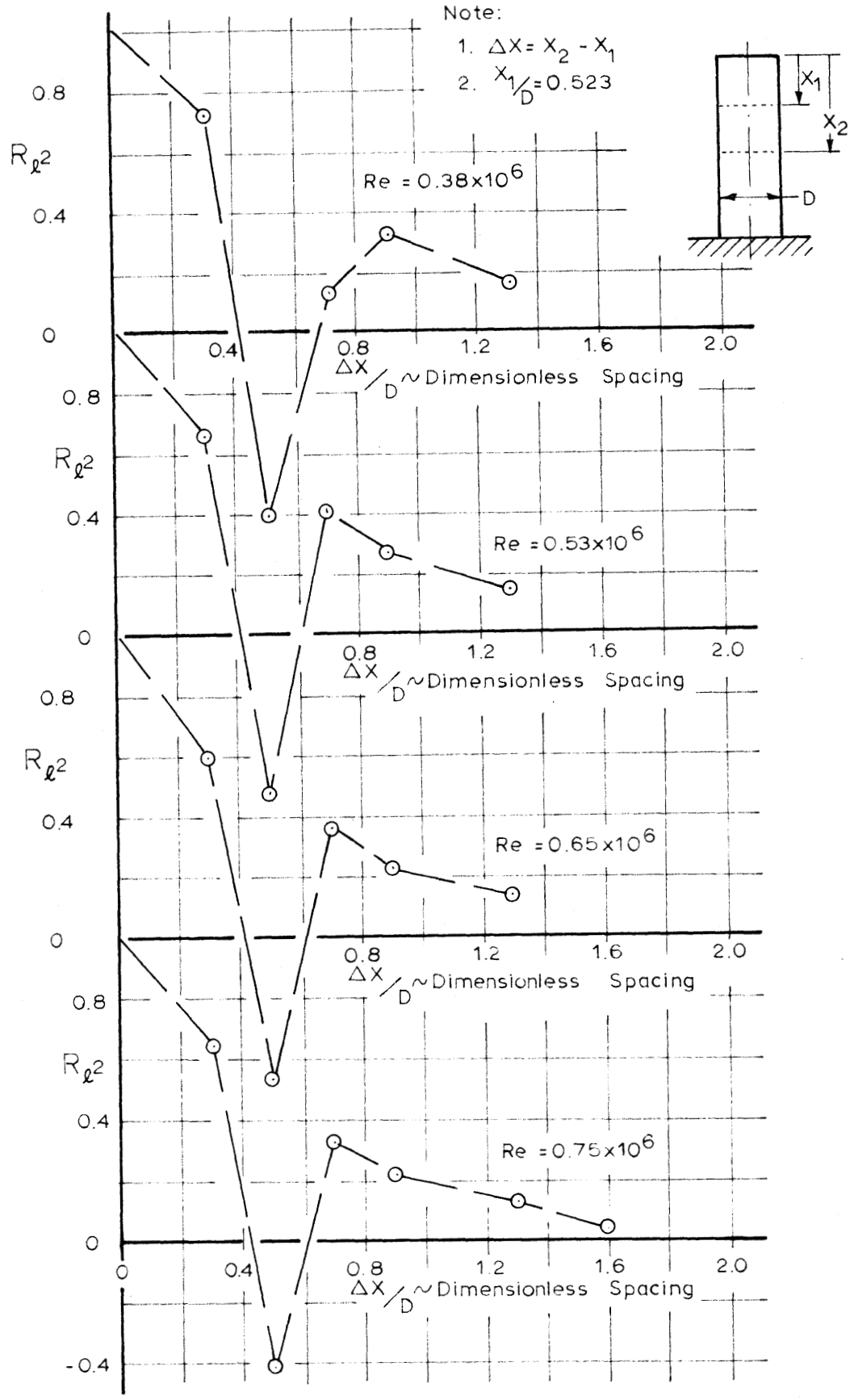


Figure 24 Lift Correlation for the Smokestack, $X_{1/D} = 0.523$

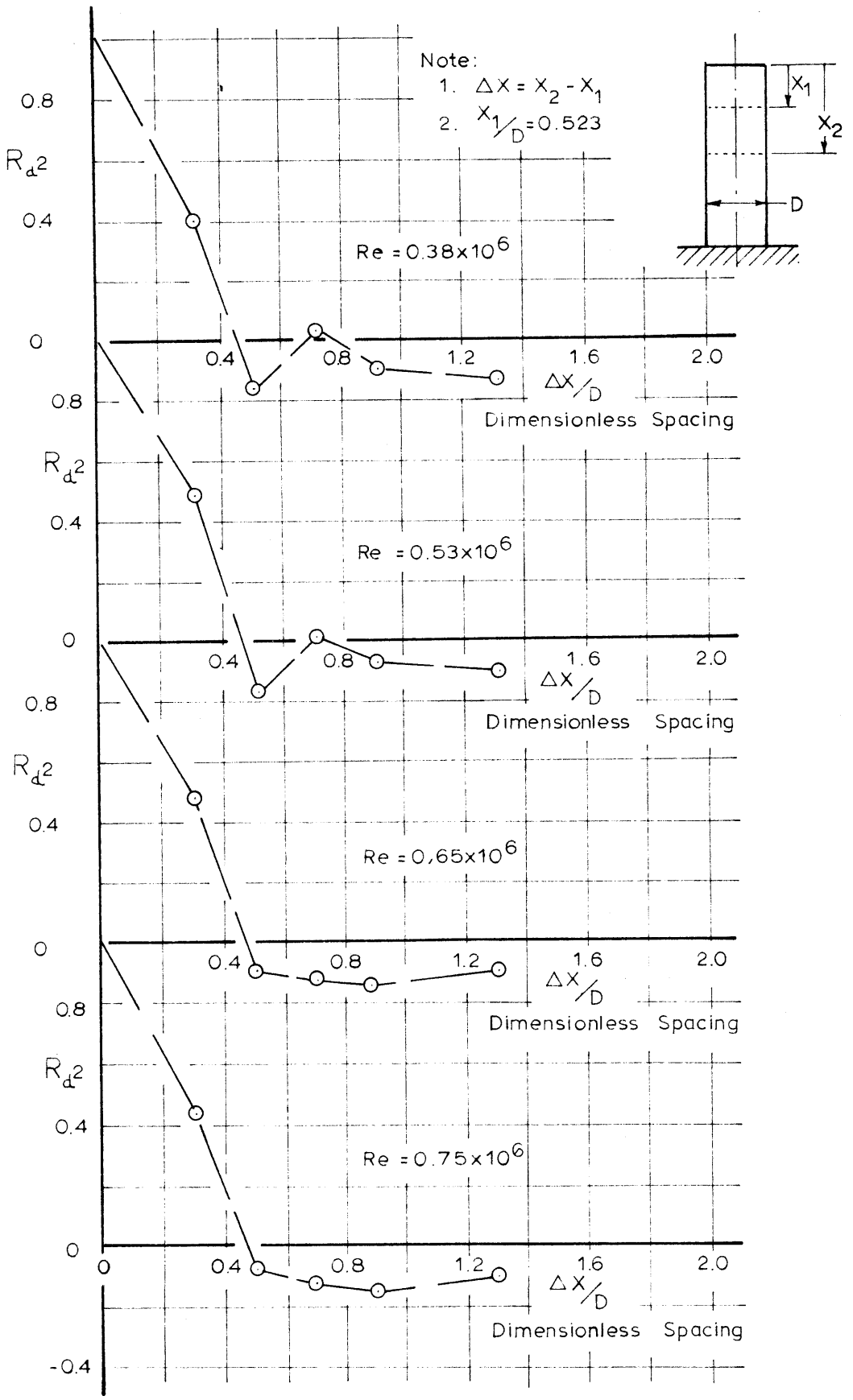


Figure 25 Drag Correlation for the Smokestack, $X_1/D = 0.523$

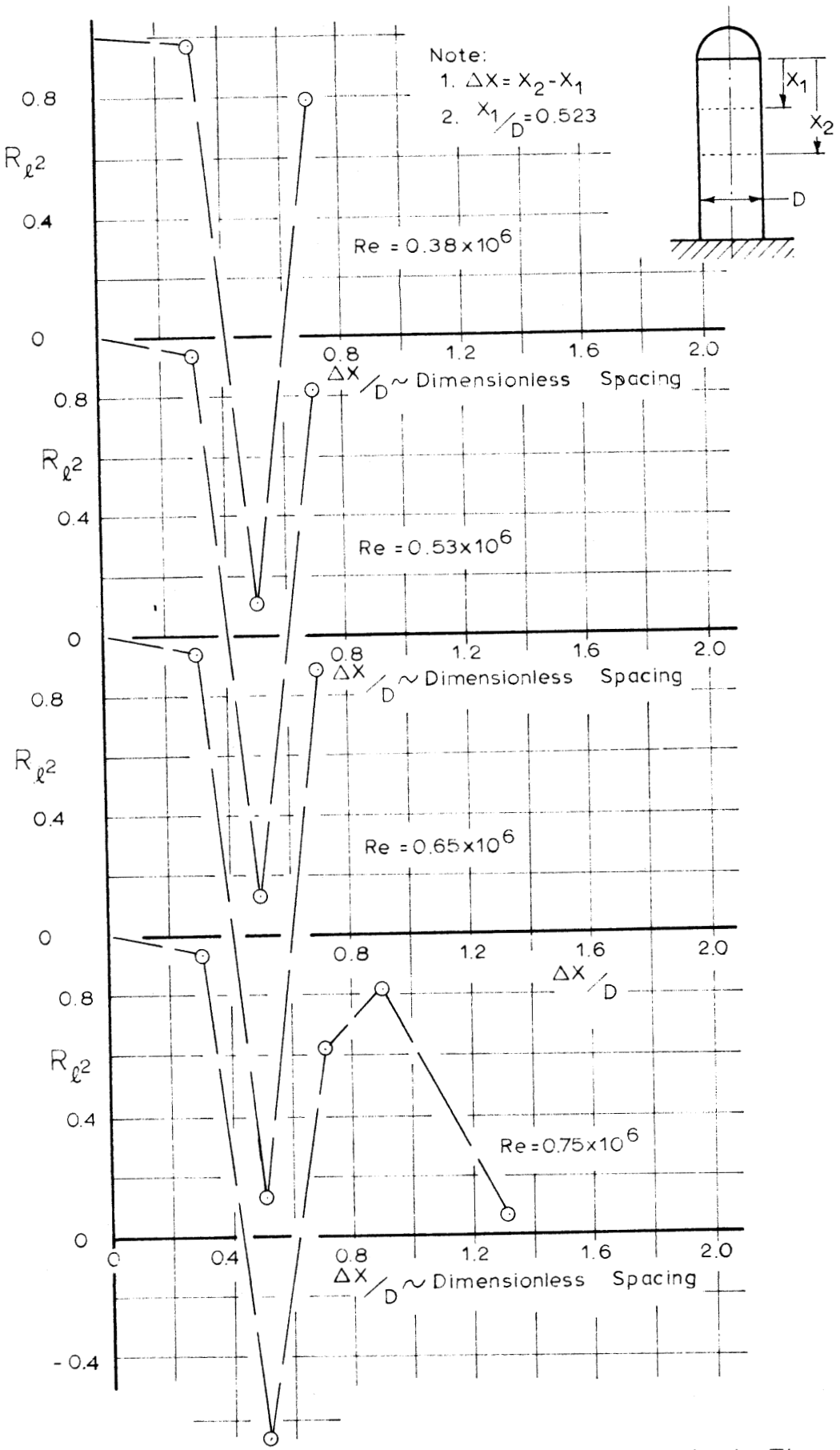


Figure 26 Lift Correlation for the Hemispherical Tip, $X_1/D = 0.523$

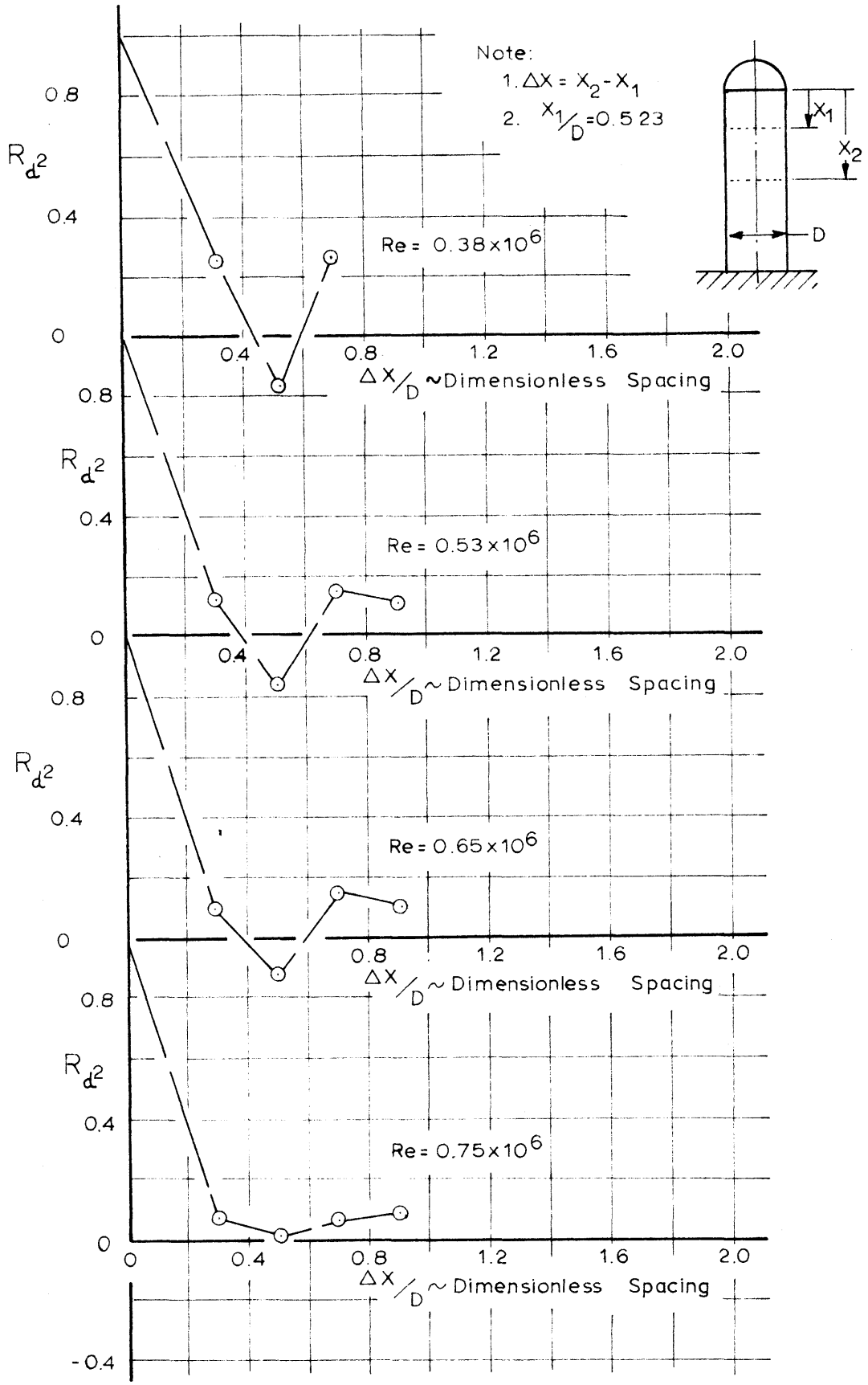


Figure 27 Drag Correlation for the Hemispherical Tip, $X_{1/D} = 0.523$

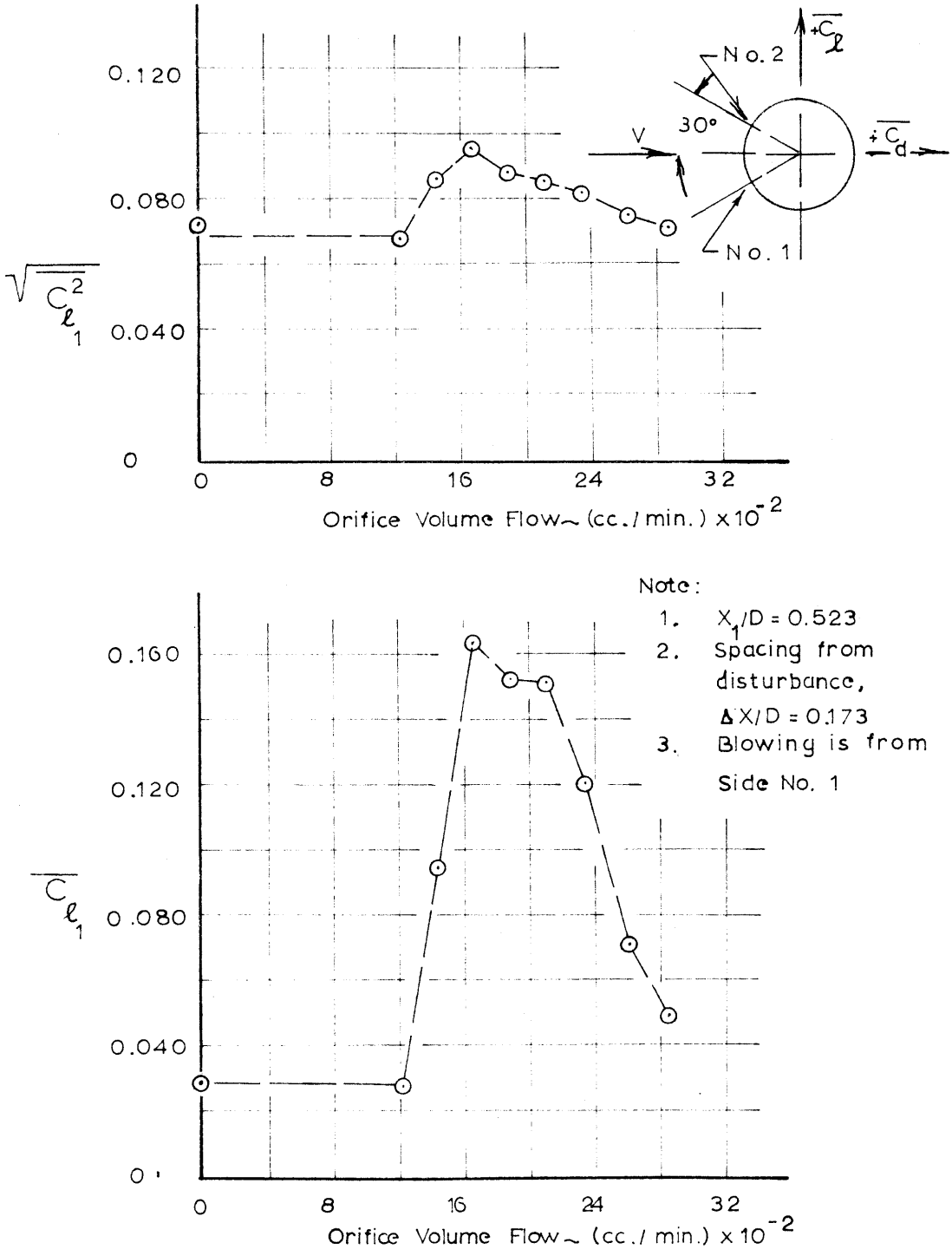


Figure 28 Effect of Asymmetrical Blowing on Lift, $Re = 0.75 \times 10^6$

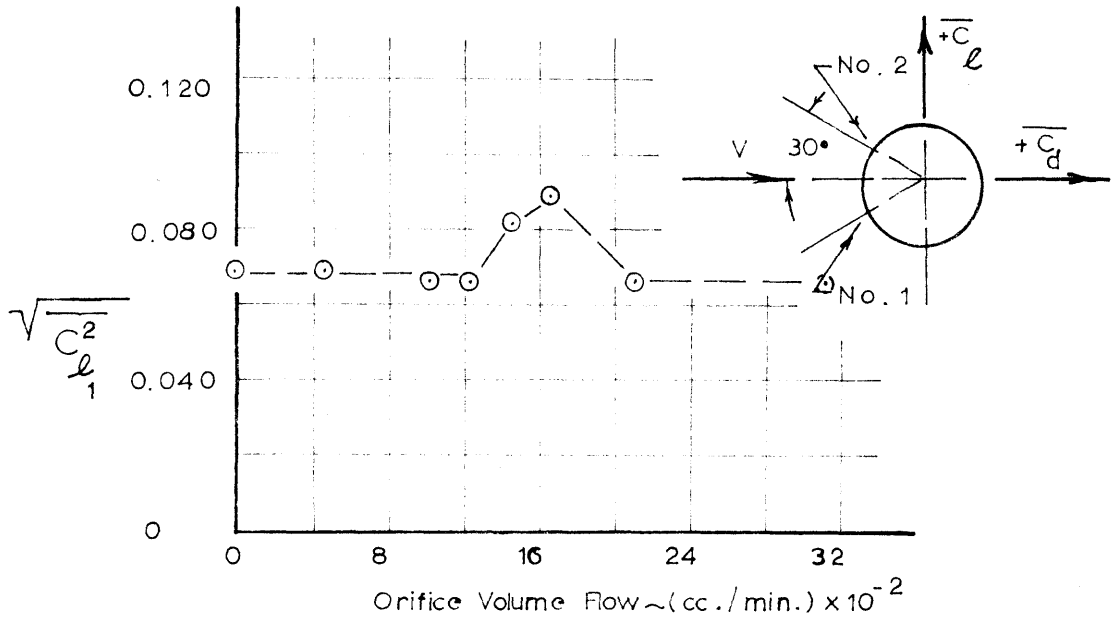


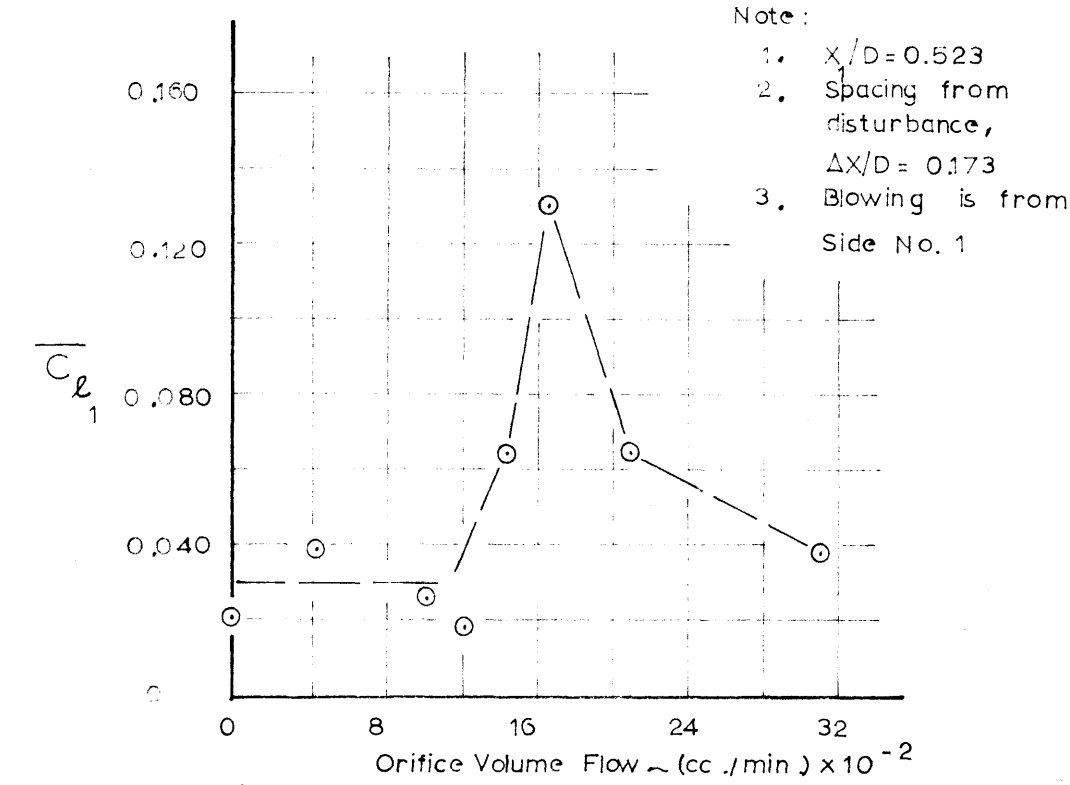


Figure 29 Effect of Asymmetrical Blowing on Lift, Re = $0.65 \times 10^6$

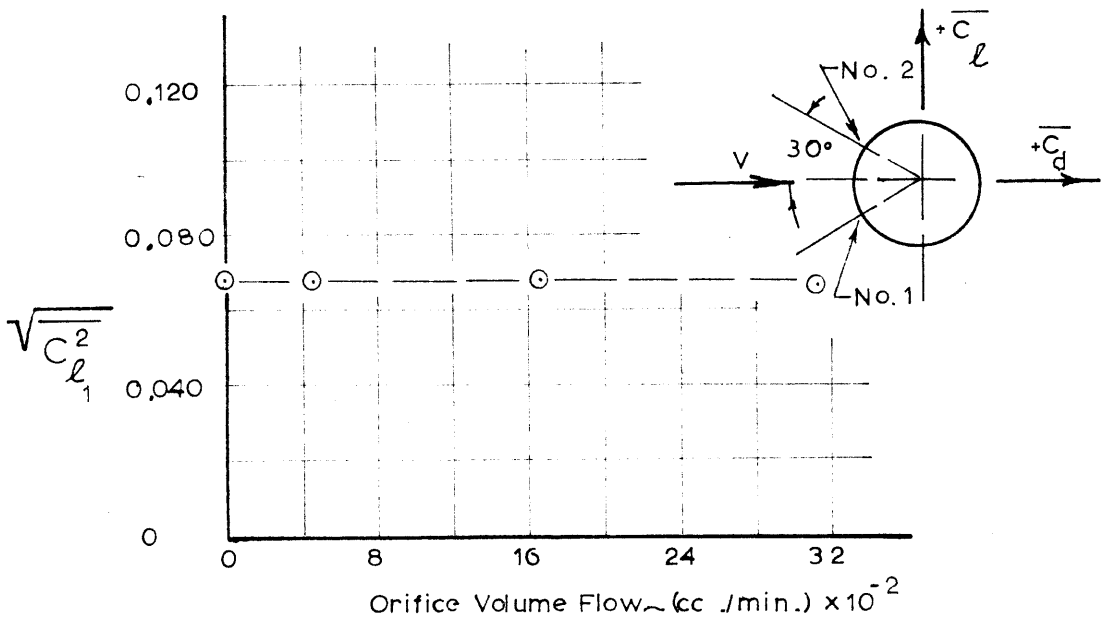


Note :

1. $X_1/D = 0.523$
2. Spacing from disturbance, $\Delta X/D = 0.173$
3. Blowing is from Side No. 1

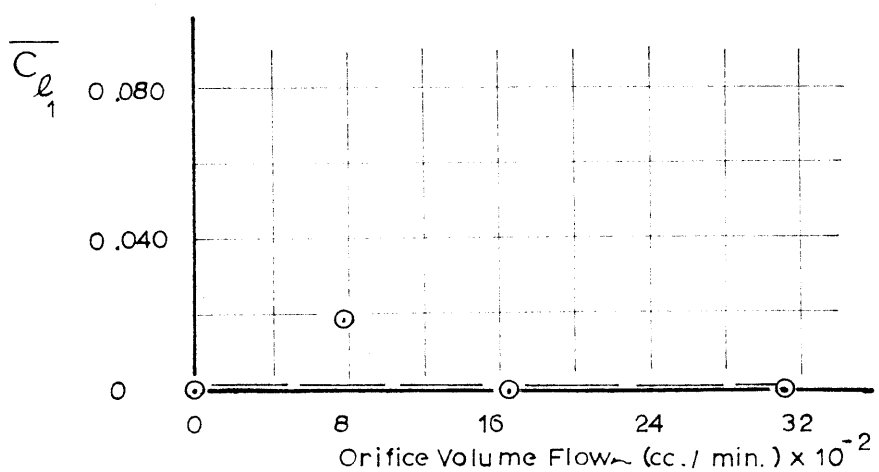


Figure 30 Effect of Asymmetrical Blowing on Lift, Re = $0.53 \times 10^6$

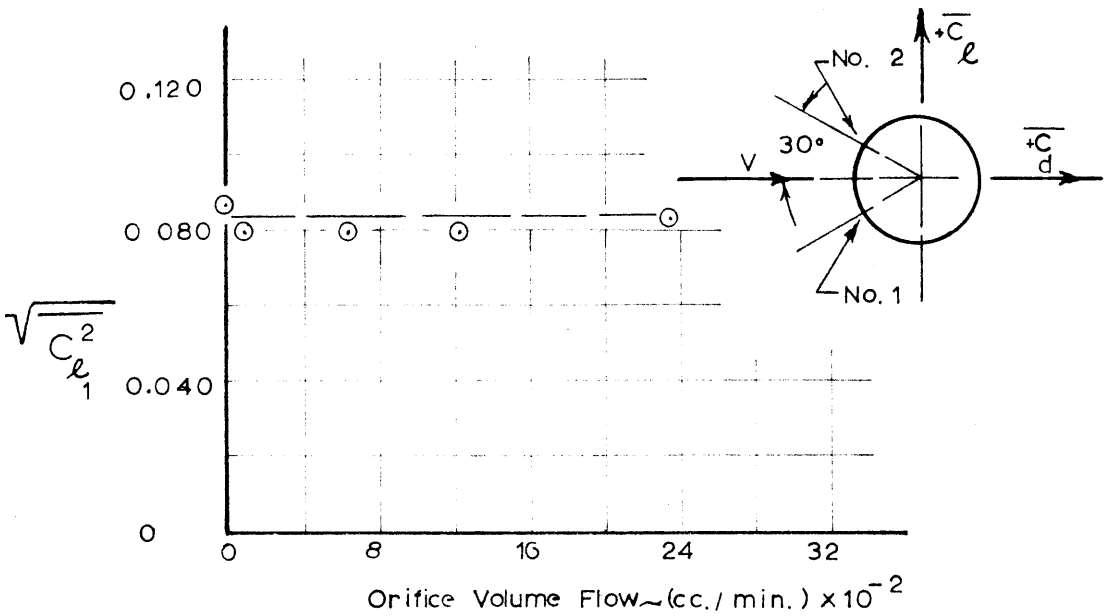


Note:

1. $X_1/D = 0.523$
2. Spacing from disturbance, $\Delta X/D = 0.173$
3. Blowing is from Side No. 1

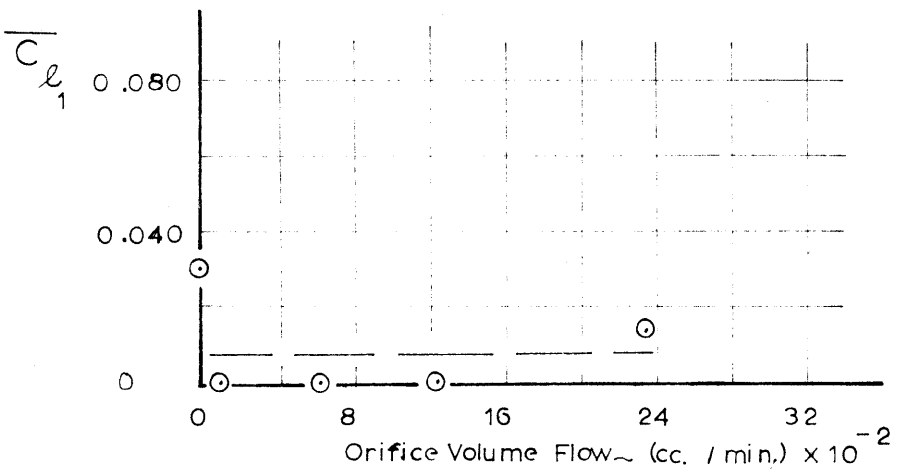


Figure 31 Effect of Asymmetrical Blowing on Lift, $Re = 0.38 \times 10^6$

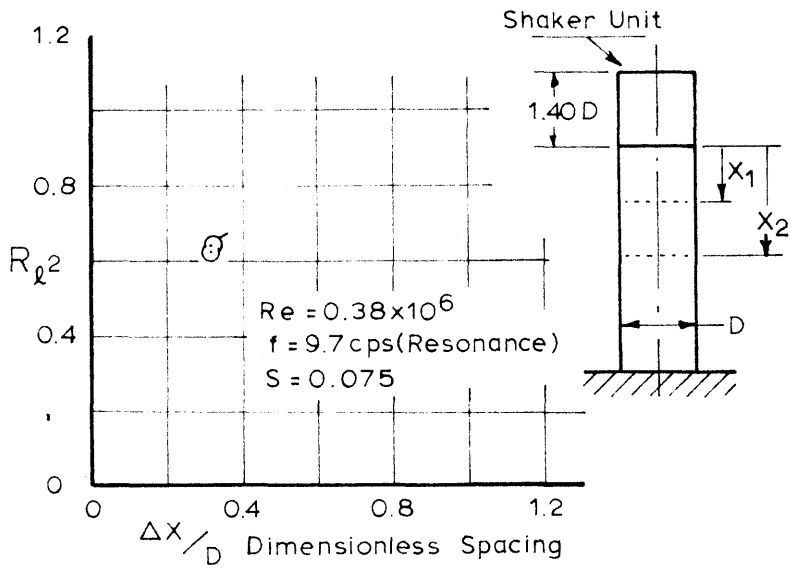


Note:

1. $\Delta X = X_2 - X_1$
2. $X_1/D = 0.523$
3. ⊙ Shaker Inoperative
   ⊘ " On

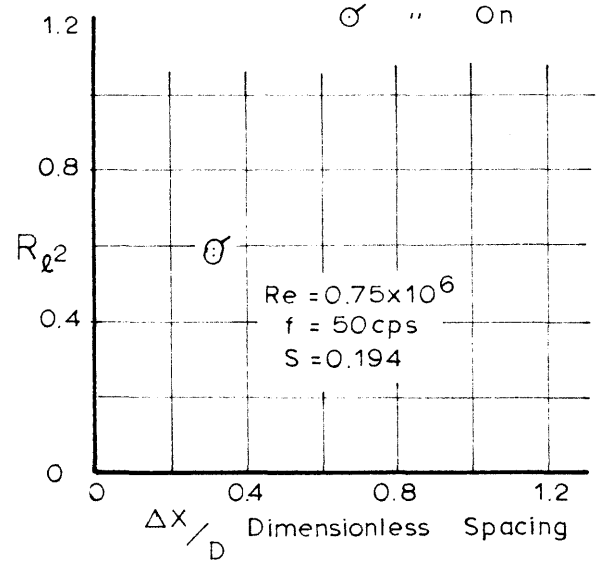


Figure 32 Lift Correlation for the Smokestack with Shaker, $X_1/D = 0.523$

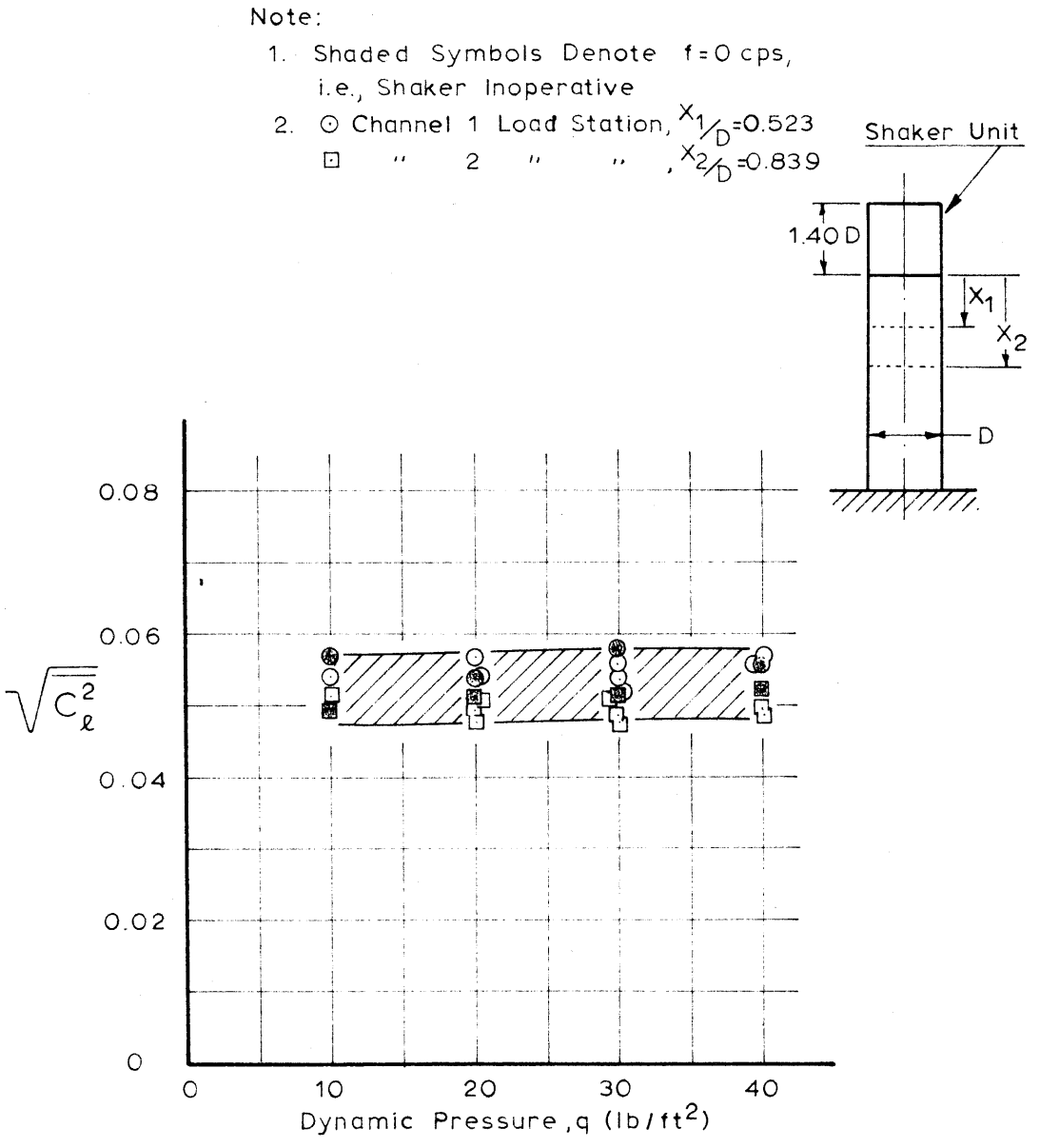


Figure 33 Effect of Shaking on Unsteady Lift